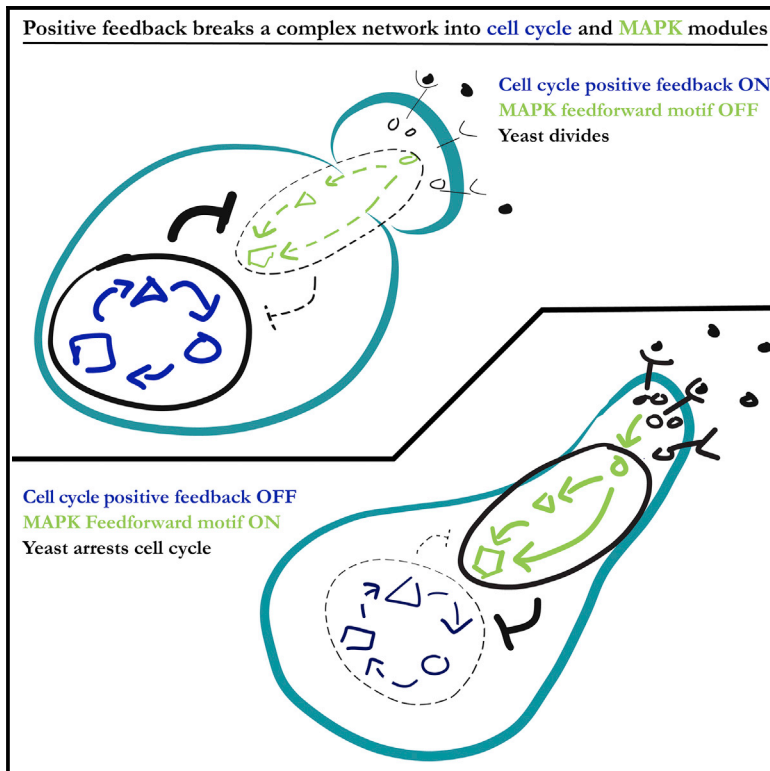


Cell Systems

Switch-like Transitions Insulate Network Motifs to Modularize Biological Networks

Graphical Abstract



Authors

Oguzhan Atay, Andreas Doncic,
Jan M. Skotheim

Correspondence

skotheim@stanford.edu

In Brief

Switch-like elements, such as positive feedbacks, insulate seemingly connected pathways and motifs from each other to allow a modular network analysis.

Highlights

- Motif analysis is valid when networks are modular
- A feedforward motif in the MAPK pathway is insulated from cell-cycle inputs
- Positive feedback insulates MAPK and cell-cycle modules in budding yeast
- Positive feedback insulates motifs by converting analog inputs to digital outputs

Switch-like Transitions Insulate Network Motifs to Modularize Biological Networks

Oguzhan Atay,¹ Andreas Doncic,¹ and Jan M. Skotheim^{1,*}

¹Department of Biology, Stanford University, Stanford, CA 94305, USA

*Correspondence: skotheim@stanford.edu

<http://dx.doi.org/10.1016/j.cels.2016.06.010>

SUMMARY

Cellular decisions are made by complex networks that are difficult to analyze. Although it is common to analyze smaller sub-networks known as network motifs, it is unclear whether this is valid, because these motifs are embedded in complex larger networks. Here, we address the general question of modularity by examining the *S. cerevisiae* pheromone response. We demonstrate that the feedforward motif controlling the cell-cycle inhibitor Far1 is insulated from cell-cycle dynamics by the positive feedback switch that drives reentry to the cell cycle. Before cells switch on positive feedback, the feedforward motif model predicts the behavior of the larger network. Conversely, after the switch, the feedforward motif is dismantled and has no discernable effect on the cell cycle. When insulation is broken, the feedforward motif no longer predicts network behavior. This work illustrates how, despite the interconnectivity of networks, the activity of motifs can be insulated by switches that generate well-defined cellular states.

INTRODUCTION

In the past few decades, a large body of work has identified many components of signaling networks, ordered them in pathways, and determined many of their biochemical interactions (Gerhart, 1999; Perrimon et al., 2012). However, it has remained difficult to use this molecular knowledge to accurately predict protein activities and cell behavior. This is primarily because there are simply too many protein interactions for which the kinetic parameters are not known, and many of these are nonlinear (Boone et al., 2007; Yosef and Regev, 2011). Thus, despite the vast increase in our knowledge of molecular interactions, how cells process information (i.e., how biological networks integrate dynamic signals to determine cellular responses) remains poorly understood.

Although it is very difficult to analyze a signaling network in its entirety, separate timescales of biological interactions often allow complex networks to be broken into sub-networks that can be analyzed independently (Alon, 2006). For example, phosphorylation kinetics are usually very fast compared with protein synthesis and corresponding concentration changes. In a network that contains both protein synthesis and phosphoryla-

tion reactions, protein concentrations can be treated as fixed when analyzing phosphorylation kinetics. Conversely, phosphorylation kinetics will be at steady state on the slower timescale of protein concentration changes. Thus, separation of timescales can enable the separation of complex networks into smaller sub-networks.

Although the separation of timescales simplifies the analysis of signaling networks, resulting sub-networks often remain too large to be experimentally tractable. Another method to study how cells process information is to partition networks into smaller, more analytically manageable parts known as network motifs (Alon, 2007b). Motifs, such as feedforward, negative feedback, and positive feedback loops, have been extensively analyzed, and their functions enumerated (Ferrell and Xiong, 2001; Ma et al., 2009; Mangan and Alon, 2003; Yosef and Regev, 2011). Indeed, motif analysis has been used in hundreds of studies to understand a diverse set of functions, from noise filtering in bacteria to stem cell differentiation (Alon, 2007b; MacArthur et al., 2009; Narula et al., 2012; Norman et al., 2013; Tsang et al., 2007). Knowledge of motif functions has also been used to construct synthetic circuits, including temperature-insensitive clocks, multicellular pattern generators, and multiplexers (Basu et al., 2004; Hussain et al., 2014; Regot et al., 2011).

However, a large fraction of synthetic motifs do not behave as expected when connected to a larger network (Gyorgy and Del Vecchio, 2014). This is because network motifs are always embedded within a larger network, which can change motif dynamics and function. Because isolated motif analysis does not consider the effect of all interacting components from the larger network, the dynamics of the motif can deviate drastically from theoretical expectations (Guet et al., 2002). For instance, we consider the case in which two proteins, X and Y, repress each other nonlinearly so that the binding of at least two X and Y molecules is necessary for repression. This double-negative feedback motif is expected to result in a bistable system with low-X, high-Y and high-X, low-Y stable steady states (Figure 1A). However, even a slight increase in network complexity by adding a single interaction can completely change the dynamics of this double-negative feedback motif. For example, if X also represses another protein Z, which in turn represses Y, the bistable system can turn into a relaxation oscillator. In this case, X and Y continuously oscillate, and there are no steady states (Figure 1B). Thus, if the addition of a single protein into a two-protein double-negative feedback motif can completely change its function, when and how can motif analysis be applied to large interconnected biological networks (Figure 1C)?

It has previously been suggested that motif analysis can be usefully applied if the network is modular, by which we mean

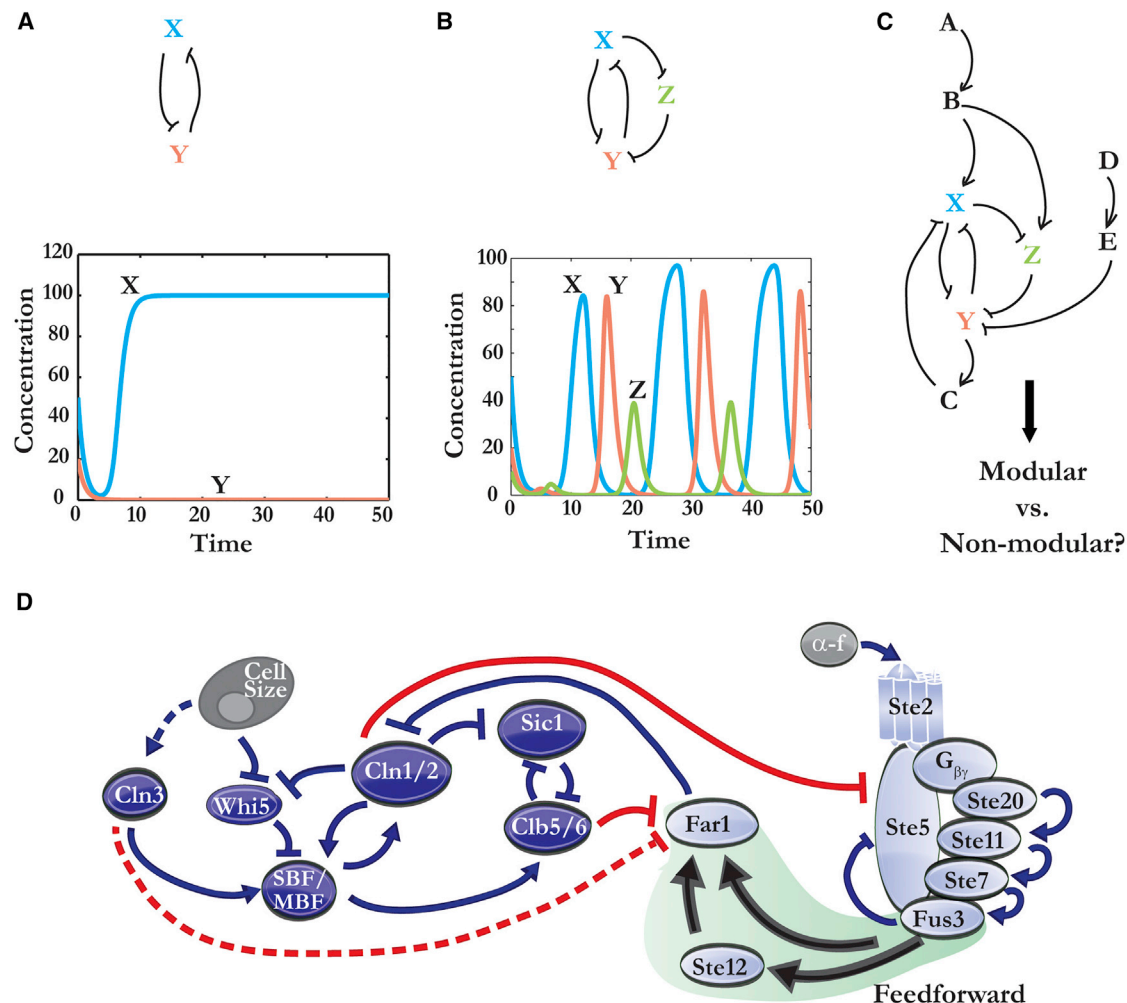


Figure 1. It Is Not Clear Why Motif Analysis Is Valid for Complex Biological Networks

(A) Schematic and simulated dynamics of a double-negative feedback loop with nonlinearity. The resulting system has two stable fixed points: high X and low Y, and high Y and low X. The equations for X and Y are $dx/dt = (1/(k^2 + y^2)) - x$ and $dy/dt = (1/(k^2 + x^2)) - y$, where $k = 0.1$.

(B) Schematic and simulated dynamics of a three-node system, where another node, Z, was added to the double negative feedback loop from (A). Even if parameters and forms of interactions from (A) are unchanged, the system exhibits sustained oscillations after the addition of Z. The equation for Z is $dz/dt = (1/(k^2 + x^2)) - z$, and Y is repressed by Z so that $dy/dt = (1/(l^2 + z^2))(1/(k^2 + x^2)) - y$, where $l = 0.01$.

(C) Schematic of a larger biological network in which (A) or (B) are sub-networks (motifs). In a larger network, it is unclear where to draw the line in terms of how many components to include in a reduced motif-based model. That is, it is not clear whether the resulting network is modular or non-modular (i.e., whether or not any sub-networks can be isolated for separate analysis).

(D) Schematic of the cell cycle G1/S network (dark purple) and pheromone pathway (light purple) in which the Fus3-Ste12-Far1 coherent feedforward motif (shaded green) is embedded. The interactions through which the cell-cycle pathway inhibits the pheromone-induced MAPK pathway to potentially break network modularity are shown in red. Upstream inputs, cell size and α -factor, respectively, are shown in gray.

that it can be broken up into discrete “modules,” or functional units on the scale of a few proteins (Hartwell et al., 1999). However, the concept of modularity has remained largely philosophical, and it is unclear what conditions are required for motif-based analyses to be valid or why many documented natural motifs behave modularly. The widespread presence of network motifs within natural systems suggests that biological networks may have specific characteristics that modularize them. Importantly, motifs often do not work similarly well in synthetic networks, as synthetic motifs require extensive empirical optimization to produce the desired behavior. Thus, synthetic biologists

may be missing some design principles that natural systems implement. Determining these design principles may greatly simplify and accelerate the construction of complex synthetic circuits to perform diverse functions.

To investigate the network design principles necessary for modularity, we used a well-studied budding yeast network: the pheromone response. This network contains a feedforward motif that arrests the cell cycle under particular conditions. Here, we define “feedforward” to mean that a network motif contains an upstream molecule (here Fus3, a mitogen-activated protein kinase [MAPK]) that modulates the activity of a downstream

molecule (here Far1, a cell-cycle inhibitor) through two branches of a pathway. In the case of this budding yeast network, the feedforward motif is understood to convey specific, discrete functions to the larger network (discussed below, and see [Doncic and Skotheim, 2013](#)). Most broadly, this work asks how the structure of this larger network insulates the feedforward motif into a single functional module so that its isolated analysis matches its predicted behavior.

The budding yeast uses the MAPK pathway to sense and respond to mating pheromone secreted by neighboring cells. The cell bases its decision to mate not only on the current extracellular pheromone concentration but also on its memory of past pheromone concentrations ([Doncic and Skotheim, 2013](#)). Arrested cells also maintain the ability to rapidly enter the cell cycle if the extracellular pheromone quickly disappears. The ability of yeast to simultaneously remember past pheromone exposure over long timescales and respond quickly to rapid changes in the extracellular concentration has been attributed to the feedforward motif discussed above, which is embedded within the MAPK pathway ([Doncic and Skotheim, 2013](#)) ([Figure 1D](#)).

Upstream of the feedforward motif, pheromone binds a receptor to trigger a cascade of rapid phosphorylation events terminating in the activation of Fus3 ([Bardwell, 2004](#); [Chen and Thorner, 2007](#)). Fus3 activity increases with pheromone concentration over a wide range and rapidly responds to any change in extracellular pheromone concentration ([Yu et al., 2008](#)). As a part of the feedforward motif, Fus3 promotes the activity of Far1 both directly, by rapid phosphorylation, and more slowly, by increasing its synthesis via the Ste12 transcription factor ([Chang and Herskowitz, 1990](#); [Errede and Ammerer, 1989](#); [Gartner et al., 1998](#); [Henchoz et al., 1997](#); [Oehlen et al., 1996](#)). Thus, the current Fus3 activity determines both the synthesis rate of Far1 and the fraction of Far1 that is activated by phosphorylation.

The feedforward relationship between Fus3 activity and Far1 has specific functional consequences for the decision to reenter the cell cycle. When Far1 is phosphorylated and active, it binds and inhibits the cyclin-Cdk complexes required to drive progression into the cell cycle ([Pope et al., 2014](#)); this prompts cell-cycle arrest in G1. Far1 is expressed at low levels in the absence of pheromone so that the cell is sensitive to small increases in pheromone-dependent Fus3 kinase activity. An increase in Fus3 kinase activity leads to a rapid increase in the concentration of phosphorylated, active Far1, which results in cell-cycle arrest ([Doncic and Skotheim, 2013](#); [McKinney and Cross, 1995](#)). Similarly rapid dephosphorylation kinetics ensures that Far1 can be quickly inactivated should pheromone disappear. Although the initial cell-cycle arrest dynamics depend on the rapid kinetics of Far1 activation, the duration of the cell-cycle arrest depends primarily on the concentration of the activated Far1 pool. Further, because the Far1 synthesis rate is dependent on the pheromone concentration through Fus3 activity ([Doncic and Skotheim, 2013](#); [Takahashi and Pryciak, 2008](#); [Yu et al., 2008](#)), this dependence imparts cellular “memory”: cells previously exposed to higher pheromone concentrations have more Far1. Because active Far1 is determined by both the total Far1 as well as the current Fus3 activity, cells that have previously accumulated more Far1 are able to stay arrested for longer at lower pheromone concentrations. Thus, cells base their decision to reenter the cell cycle on both current and past pheromone concentra-

tions. In this way, the feedforward motif converts a dynamic Fus3 signal into Far1 activity to provide both memory and rapid response (see the [Supplemental Information](#) for detailed information on the feedforward motif and its analytical description; [Figures S1A–S1C](#)).

Even though studying Far1 in the context of the feedforward motif has been illuminating, it is unclear why this motif should behave as an independent module, because it is not biochemically isolated from the rest of the network. To the contrary, it is actively regulated by other network components ([Figure 1D](#)). Specifically, Fus3 activity inhibits upstream MAPK pathway components through negative feedback, and cyclin-dependent kinase activity from the cell-cycle pathway inhibits Far1 and the MAPK scaffold protein Ste5 ([Bhattacharyya et al., 2006](#); [Garrenton et al., 2009](#); [Strickfaden et al., 2007](#); [Yu et al., 2008](#)). Here, we resolve this conundrum. We show that modularity of the feedforward motif results from the presence of multiple positive feedbacks that convert an analog input (cyclin-Cdk activity) into an ON/OFF digital output (cell-cycle reentry). In the OFF state, feedforward motif dynamics are effectively insulated from the cell cycle, and their behavior dominates the cell’s response to pheromone, whereas in the ON state, cyclin-Cdk1 activity dominates, the cell cycle is initiated, and the feedforward motif is dismantled. Because many cellular decisions are switch-like, we expect this to be one of many examples in which switch-like transitions modularize complex biological networks.

RESULTS

The Feedforward Motif Regulating Far1 Is Insulated from the Cell Cycle during Arrest

That the feedforward motif analysis predicts cellular behavior suggests a modular network structure. Evidence for this is described above and further detailed in the supporting material and [Figure S1](#). Specifically, the nuclear Far1 concentration gradually increases in arrested cells that are exposed to constant intermediate pheromone concentrations, consistent with the feedforward motif model. Then, it is rapidly degraded at cell-cycle reentry ([Figures S1G and S1H](#); [Doncic and Skotheim, 2013](#)). This is in stark contrast to what would be expected from a gradually increasing cell-cycle signal gradually increasing the degradation rate of Far1 (compare [Figures S1G and S1H](#) with [Figures S1B and S1E](#)). This suggests that the feedforward motif is insulated from the cell-cycle signal during arrest.

The power of motif analysis is that it is able to predict the system’s response to any dynamic input signal, no matter how complex. If the feedforward motif is indeed insulated, the simulation of motif dynamics should be able to predict Far1 dynamics even for dynamic extracellular pheromone concentrations. To test this, we exposed cells to either a series of alternating 2 hr 12 nM pulses and 1 hr 3 nM pulses of extracellular pheromone or a step increase to constant 12 nM pheromone using microfluidics, as previously described ([Doncic et al., 2011, 2013](#)) ([Figures 2A–2C](#)). In these cells, we measured nuclear Far1 dynamics by a Far1-GFP fusion protein expressed from its endogenous locus and Whi5-mKok fusion protein that was used to identify the G1 cell cycle phase and the nucleus ([Costanzo et al., 2004](#); [de Bruin et al., 2004](#); [Doncic et al., 2011](#); [Tsutsui et al., 2008](#)). We focus on the nuclear pool of Far1 because it determines cell-cycle arrest.

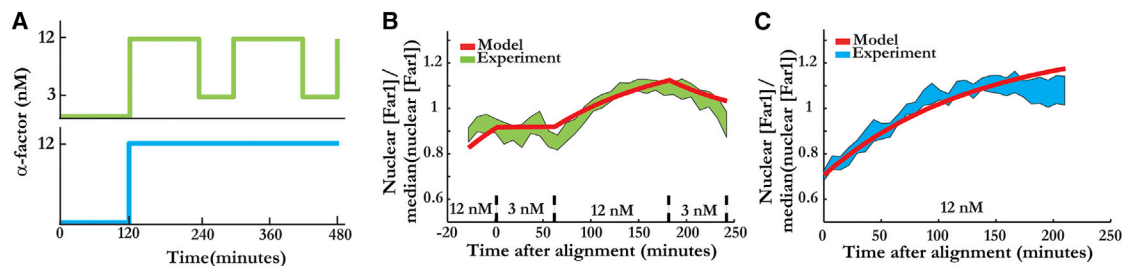


Figure 2. The Feedforward Motif Predicts Far1 Dynamics in Response to Complex Input Signals

(A) Schematic of the input signals for experiments shown in (B) (top) and (C) (bottom).

(B) Cells were exposed to an alternating series of 2 hr 12 nM and 1 hr 3 nM extracellular pheromone pulses, and nuclear Far1 was measured and compared with model results. We considered cells that were born and arrested between 1 and 1.5 hr after the beginning of the first 12 nM pheromone pulse. Traces were aligned at the beginning of the first 3 nM pulse. Shaded green denotes the region containing the mean nuclear Far1 concentration and associated SE. The red overlaid line denotes the prediction from the feedforward motif model. Note that the model was not fit to the data. The only input to the model from the experiment is the input signal (A) and the measured cell growth rate.

(C) The model and experiment comparison for cells exposed to a step increase from 0 to 12 nM pheromone. Traces were aligned at the beginning of cell-cycle arrest, as determined by the appearance of Far1 in the nucleus. In contrast to (B), the nuclear Far1 concentration steadily increases from the beginning of the experiment and stabilizes at a high steady-state concentration.

When cells were exposed to series of alternating pulses of pheromone, Far1 concentration did not drop after the first 3 nM pulse but did drop during the second 3 nM pulse. According to the model, this is because during the first pulse, dilution, a product of current Far1 concentration and cell growth rate, is balanced by Far1 synthesis. During the second 3 nM pulse, Far1 has already increased to a higher concentration so that the dilution/degradation term is larger than the synthesis term, and the Far1 concentration decreases. In contrast, when cells were exposed only to 12 nM pheromone, Far1 monotonically increased toward a steady-state concentration (Figure 2C). The good agreement between model and experiment further supports the hypothesis that the feedforward motif is effectively insulated from the cell cycle.

The Cell-Cycle Control Network Digitizes Gradual Analog Input Signals

Modularity requires that we be able to separately consider the upstream pheromone pathway components, the feedforward motif, and the downstream cell cycle regulatory network. The dynamics of upstream pheromone components are determined by fast phosphorylation kinetics on the minute timescale (Yu et al., 2008). This means that the activities of these components are in steady state on the hour-long timescales of protein accumulation and cell-cycle progression. Thus, the upstream pheromone pathway dynamics should be separate from the feedforward motif because of a separation of timescales. However, it is unclear why the dynamics of the feedforward motif could be usefully modeled without considering the effect of the cell-cycle signal, which is likely to be gradually increasing during arrest as the cells get larger.

To understand why the feedforward motif is insulated from the cell-cycle signal, we decided to examine the dynamics of the cell-cycle signal during pheromone arrest to determine how cells drive cell-cycle reentry. Although the concentration dynamics of cell-cycle proteins in cycling cells have recently been reported (Schmoller et al., 2015), it is not clear if the dynamics of these proteins are the same in pheromone-arrested cells. Thus, we examined the dynamics of cell-cycle proteins

in cells that are exposed to a step increase in pheromone up to an intermediate concentration (3 nM α -factor). At low to intermediate pheromone concentrations, cells initially arrest and prolong their G1 before eventually reentering the cell cycle (Doncic and Skotheim, 2013).

In both cycling and pheromone-arrested cells, upstream signals triggering cell division that are driven by cell growth are expected to change slowly and to operate on the timescale of the cell growth rate (Figures 3A and 3B). The main way cell growth triggers division is through the upstream G1 cyclin Cln3 and the cell-cycle inhibitor Whi5. In cells cycling without pheromone, Whi5 is diluted during G1 by cell growth, while Cln3 concentration is constant (Schmoller et al., 2015). While Cln3 concentration is constant in cycling cells, this may not be the case in pheromone-arrested cells. We therefore measured Cln3 concentration during a pheromone-induced cell-cycle arrest. Because the concentration of wild-type (WT) Cln3 cannot be measured using fluorescence microscopy because of its rapid and constitutive degradation (Tyers et al., 1992), we examined a mutant strain expressing a stabilized, more abundant, but less active Cln3 protein previously characterized and used to examine G1/S cell cycle regulation (*mCitrine-CLN3-11A*) (Bhaduri and Pryciak, 2011; Liu et al., 2015; Schmoller et al., 2015). In contrast to freely cycling cells, in which Cln3-11A was measured to be constant (Schmoller et al., 2015), Cln3-11A concentration gradually increased during pheromone-induced arrest on a similar timescale as cell growth (Figures 3C and 3D). This observation is consistent with a previous fluorescence in situ hybridization measurement that found the mean number of Cln3 mRNA to increase during pheromone arrest (Doncic and Skotheim, 2013). Cln3 has been suggested to directly inhibit Far1 (Alberghina et al., 2004). If this were true, the gradual increase in Cln3 would break modularity so that the feedforward motif could not be analyzed independently of Cln3. However, our observation of Far1 stability during arrest suggests that Cln3-dependent destabilization of Far1 is relatively unimportant during pheromone arrest.

Next, we analyzed the concentration dynamics of the cell-cycle inhibitor Whi5, the primary target of Cln3. In contrast to

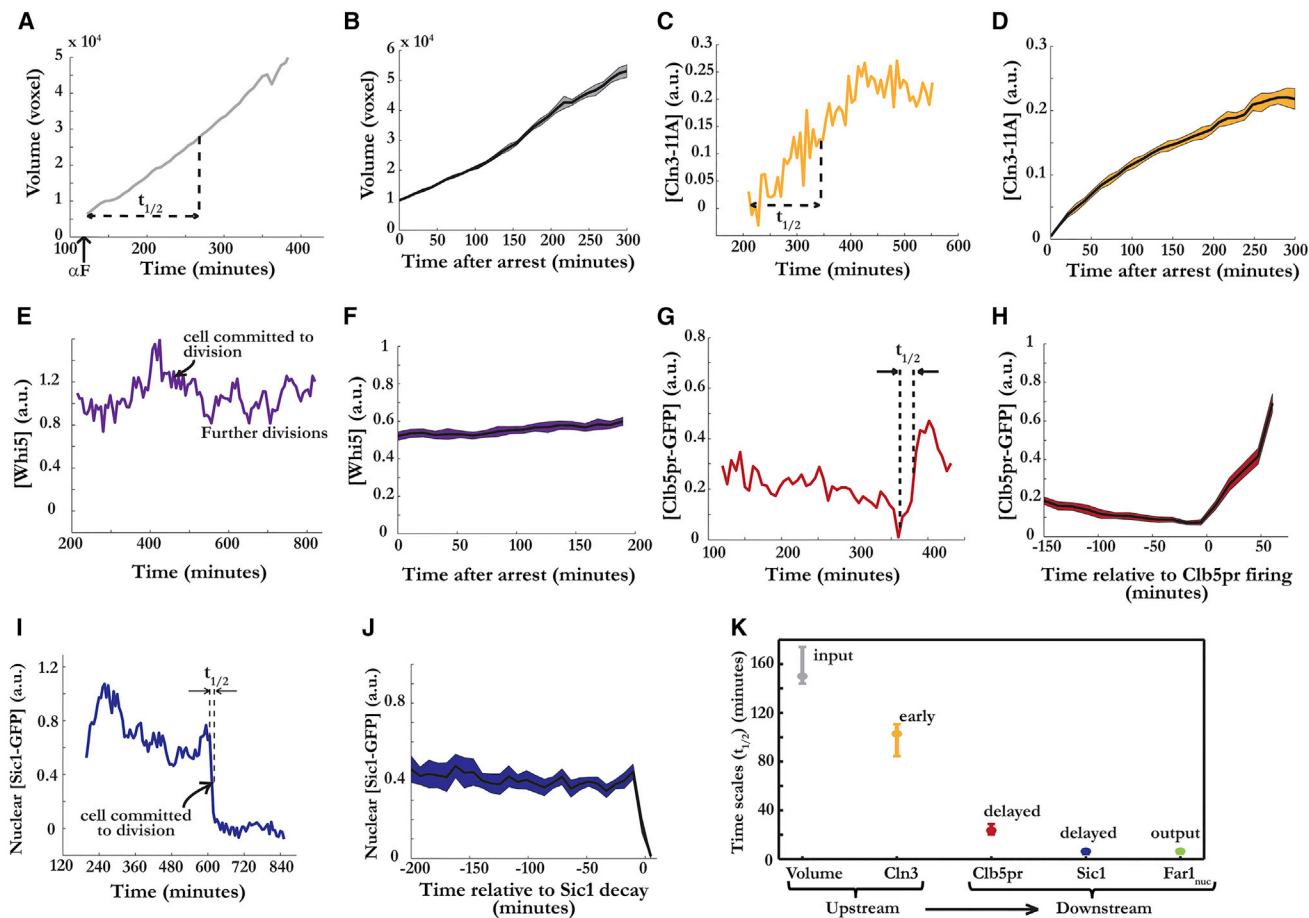


Figure 3. Timescales of Cell-Cycle Proteins Get Progressively Shorter as the Signal Moves from Upstream Inputs to Downstream Positive Feedback Elements

(A and B) Example (A) and mean single-cell traces of volume (B) for cells aligned at the start of arrest. Volume increases approximately linearly during pheromone arrest, in agreement with previous measurements in similar conditions (Gorantov et al., 2009). (C and D) Example (C) and mean single-cell traces of mCitrine-Cln3-11A concentration (D) for cells aligned at the start of arrest. Expression of the upstream cyclin Cln3 gradually increased during pheromone arrest. (E and F) Example (E) and mean single-cell traces of the cell-cycle inhibitor Whi5-mKok (F) for cells aligned at the start of arrest. Whi5 concentration was constant in cells exposed to 3 nM pheromone. (G and H) Example (G) and mean single-cell traces (H) of a transcription reporter (*CLB5pr-GFP*) for the synthesis of the downstream cyclin Clb5. Single-cell traces were aligned at the activation of the integrated *CLB5* promoter expressing GFP. (I and J) Example (I) and mean single-cell traces of Sic1-GFP (J), a stoichiometric inhibitor of Clb5-Cdk complexes. Single cells were aligned at cell-cycle reentry, which is coincident with Sic1 degradation. (K) The timescales of volume increase, Cln3-11A upregulation, Clb5 synthesis, Sic1 degradation, and nuclear Far1 degradation during pheromone arrest. Timescales get progressively shorter as one moves from cell-cycle inputs (e.g., volume increase and Cln3) to downstream elements such as Sic1 degradation. In (B), (D), (F), (H), and (J), cell-specific fluorescence background was subtracted before averaging the single-cell traces, and shaded intervals indicate SEM. The timescale for nuclear Far1 degradation is obtained from the data shown in Figures S1G and S1H. Bars in (K) denote 90% confidence intervals for median computed using 10,000 bootstrap simulations ($p < 0.001$ for all pairwise comparisons except for Sic1 versus Far1_{nuc}).

cycling cells, for which Whi5 dilution is the primary trigger for G1/S transition (Schmoller et al., 2015), Whi5 concentration was relatively constant in cells arrested in 3 nM pheromone (Figures 3E and 3F). This can be explained by the fact that the Whi5 synthesis rate is independent of cell size (Schmoller et al., 2015) and that the rate of volume increase is lower in pheromone-arrested cells than cycling cells (Gorantov et al., 2009). Thus, at intermediate pheromone concentrations, Whi5 synthesis is balanced by cell growth. At saturating pheromone concentrations, cells form multiple shmoo and grow even more slowly, such that

Whi5 concentration can even increase over time (Figure S2). The gradual increase in Whi5 concentration in these conditions likely contributes to the fact that the vast majority of these cells never reenter the cell cycle. At intermediate pheromone concentrations, however, cells gradually increase Cln3 relative to Whi5 during arrest to drive cell-cycle reentry. The related G1 cyclins Cln1 and Cln2, although crucial for coherent cell-cycle entry in cycling cells (Skotheim et al., 2008), have little effect on cell-cycle reentry kinetics in pheromone-arrested cells (Doncic and Skotheim, 2013), so we did not analyze their dynamics here.

That Far1 concentration does not decrease until cell-cycle reentry suggests that the gradually increasing upstream Cln3/Whi5 signal does not affect Far1 during pheromone arrest. This implies that Far1 stability, which abruptly decreases at cell-cycle reentry, is regulated mainly by downstream cyclin-Cdk activity. Because cells lacking Clb5, and the related cyclin Clb6, are slower in emerging from a pheromone-induced arrest (Donicic and Skotheim, 2013), we hypothesized that it is the rapid activation of these B-type cyclins that underlies the digital aspects of nuclear Far1. To examine the B-type cyclin switch, we measured *CLB5* expression and the concentration of the B-type cyclin inhibitor Sic1 (Schwob et al., 1994; Schwob and Nasmyth, 1993). We examined *CLB5* expression using a *CLB5* promoter (1 kb upstream of the gene) driving the synthesis of GFP. We observed an abrupt activation of the *CLB5* promoter near the time of cell-cycle reentry (Figures 3G and 3H). We also examined the concentration dynamics of Sic1-GFP, expressed from the endogenous locus, and found an abrupt drop in Sic1 concentration at the point of cell-cycle reentry, consistent with previous results for cells cycling in the absence of pheromone (Figures 3I and 3J) (Yang et al., 2013). The rapid increase in B-type cyclin synthesis and decrease in its inhibitor Sic1 implies a rapid increase in B-type cyclin activity that is likely to lead to a drop in Far1 stability and thereby lead to the observed steep drop in nuclear Far1. Thus, the switch-like digital aspects of B-type cyclin activation likely underlie the modularity of the network comprising cell-cycle reentry and pheromone pathways.

Switch-like Cell-Cycle Reentry Underlies Network Modularity

Our analysis so far indicates that the network regulating cell-cycle reentry is modular because of switch-like activation of B-type cyclins, which have previously been shown to degrade Far1 (Donicic et al., 2015). Prior to cell-cycle reentry, B-type cyclin-Cdk activity is virtually nonexistent because of both its low synthesis and the presence of Sic1. At the G1/S transition, B-type cyclin synthesis increases and Sic1 is degraded so that B-type cyclin activity quickly increases to destabilize Far1. Many positive feedback loops act to sharpen the G1/S switch, including positive feedback of Cln1 and Cln2 on their own synthesis, and a double-negative feedback between the B-type cyclins Clb5 and Clb6 and their inhibitor Sic1 (Köivomägi et al., 2011; Skotheim et al., 2008; Yang et al., 2013). As one approaches the point of commitment to division, timescales of activation dynamics of proteins that control the cell cycle become faster and faster, so that the amount of time taken to switch into the cell cycle is much shorter than arrest duration (Figure 3K). Thus, for the vast majority of the arrest, cell-cycle pathway activity is effectively zero and can be neglected. This enables the feedforward motif to function as an isolated module within the network controlling cell-cycle reentry. However, if downstream cyclin activation were less switch-like, or if Cln3-Cdk were able to target Far1 for degradation, we would predict the breakdown of network modularity. Thus, we hypothesized that the degree of network modularity is determined by how switch-like B-type cyclin activation is.

To determine the relationship between switch-like transitions and network modularity, we developed an ordinary differential equation model that describes the G1/S cell cycle and phero-

none pathways using five proteins and two input signals (cell size and pheromone). To construct this model, we added the inhibition of Far1 by downstream cyclins to the feedforward model (Figure 4A; see the Supplemental Information for extended mathematical description). In our simplified model, we subsume all downstream cyclin activity, including Cln1, Cln2, and Clb5 and Clb6, into a combined variable called Clb5/6. Moreover, we control how switch-like the transition is using a single parameter that combines all of the cell-cycle positive feedbacks into a single relationship between upstream cell-cycle components, Cln3/Whi5, and the downstream activation of B-type cyclins. The cell-cycle input signal Cln3/Whi5 gradually increases as cells are arrested and is modeled using graded Michaelis-Menten kinetics. Cln3/Whi5 activates Clb5/6, either gradually or sharply. We characterize the degree of how switch-like the transition is using a Hill equation with Hill coefficient, n , so that $output = (V_{max} \cdot input^n) / (input^n + K_m^n)$, where K_m is the input value at which output is half of its potential maximum, V_{max} (Figure 4B). When $n = 1$, the relationship between Cln3/Whi5 and B-type cyclin activation is graded. As n increases, so does the sharpness of the transition. It is of particular importance that for a switch-like transition, the initial increase in the input signal does not result in a significant increase in the output until a threshold level is reached. Around the threshold, output rapidly increases to a very high level. For high enough n , the switch produces an analog-to-digital conversion of the upstream signal.

Despite greatly simplifying the complexity of the G1/S cell-cycle and pheromone pathways, our minimal model still contains eight differential equations, eight initial conditions, and 18 parameters. As with any mathematical model of biological networks, we do not have accurate in vivo measurements for many of these parameters. Instead of trying to determine the values of these parameters by fitting our model to limited data, we simply chose parameters expected to be the correct order of magnitude on the basis of known cellular reaction rates (see Tables S1 and S2). The model was then simulated for 3 nM α -factor to ensure that the kinetics of different proteins were qualitatively in agreement with experimental observations (Figure S3). The model was then tested at a range of pheromone concentrations to verify that it can predict increasing arrest durations at increasing pheromone concentrations (Figure S4).

After establishing that the minimal computational model exhibits the basic features of arrest dynamics, we examined the effect of the switch parameter, n , on Far1 dynamics (Figure 4C). We compared the results of our computational model with those predicted by an isolated mathematical analysis of the feedforward motif. For this comparison, we devised a deviation metric that indicates the percentage deviation between two time-dependent Far1 curves. To account for differences in arrest duration, we calculated the deviation from the feedforward model per unit time. Then, the percentage difference for each point on two corresponding curves is found, and these values are averaged over all points. When $n = 1$, the activation of downstream cyclins was gradual, and the percentage deviation was found to be ~33% (Figures 4D and 4F). As n was increased, downstream cyclins become more and more switch-like, and the deviation between the computational model and the ideal feedforward motif consistently decreased to less than 10% for $n = 4$ and $n = 8$ (Figures 4E and 4F).

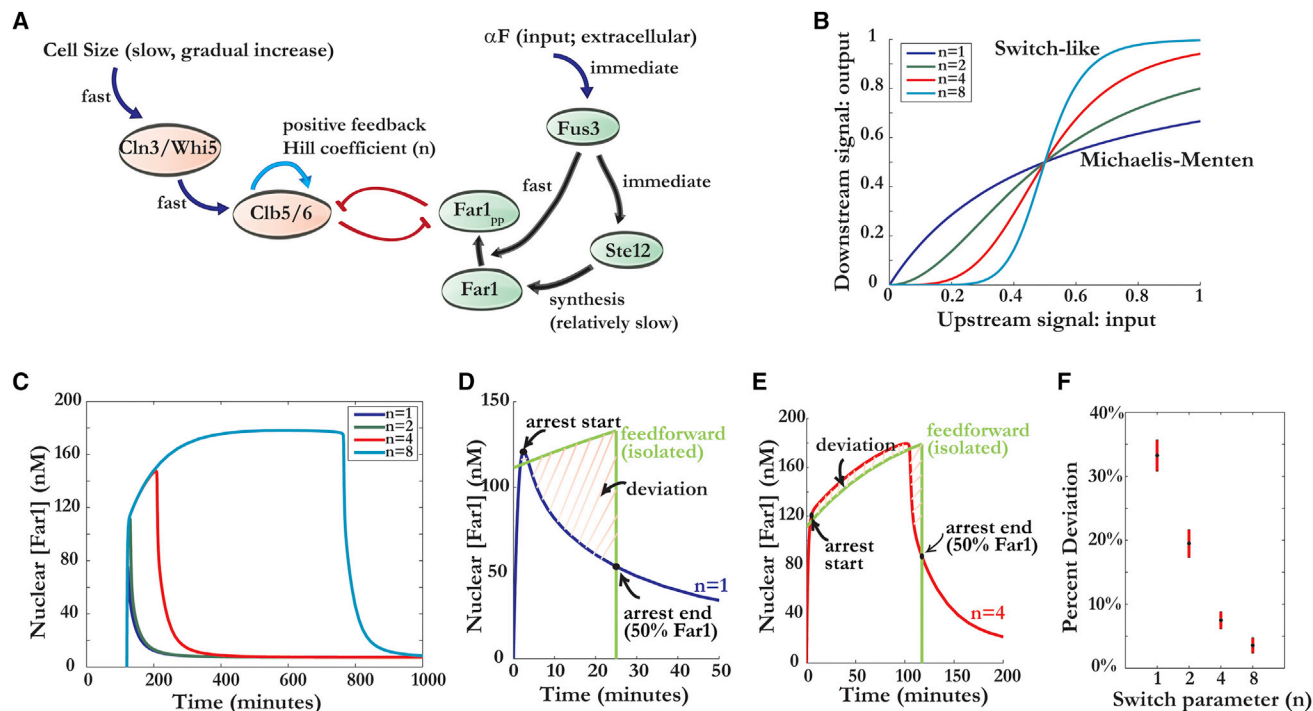


Figure 4. A Minimal ODE Model of the G1/S Cell Cycle and Pheromone Pathways Suggests that the Cell-Cycle Switch Underlies Network Modularity

(A) Schematic of the ODE model. All positive feedbacks that exist in the G1/S cell-cycle pathway are incorporated into a single positive feedback element (shown in light blue) with a single, tunable parameter, n .

(B) The switch parameter, n , determines how switch-like the cell cycle transition is. As n increases, the signal transmission becomes more and more switch-like. For higher values of n , signal transmission is digital so that nearly no downstream signal is transmitted until a threshold is reached.

(C) Far1 dynamics from simulations with increasing values of the switch parameter n for simulations at 3 nM pheromone. As n increases, simulated nuclear Far1 dynamics approach the result from an isolated motif analysis (see Figures S1A–S1C).

(D and E) Schematics of how the deviation of Far1 dynamics from the ideal motif dynamics is calculated. Arrest is taken to begin after the initial fast phosphorylation kinetics (~ 5 min) and to end when nuclear Far1 concentration reaches 50% of its peak value. Far1 levels are normalized at the start of the arrest to match the Far1 levels predicted by the isolated feedforward analysis (green), and deviation is calculated as $|Far1_{motif} - Far1_{model}| / Far1_{motif}$ for equally spaced time points between arrest start and arrest end. Examples shown are for simulations at 4 nM pheromone. (D) $n = 1$ (dark blue) (37% deviation); (E) $n = 4$ (red) (9% deviation).

(F) Deviation from ideal motif dynamics for increasing switch parameter n . Deviation was calculated for simulations at 1, 1.5, 2, 2.5, 3, 3.5, 4, 4.5, and 5 nM pheromone and the mean and SD for all simulations at the same switch parameter n are shown ($p < 0.001$ for all pairwise comparisons).

To determine the parameters affecting feedforward motif modularity, we performed a local sensitivity analysis. In this analysis, all parameter values were individually varied, and the deviation metric was recalculated. Of the 18 total parameters of the model, deviation was sensitive to only 4 parameters, including the switch parameter n , the Clb5/6 concentration required to reach half-maximum self-activation rate, the rate at which Far1 is degraded by Clb5/6, and the rate at which Far1 is activated by Fus3 (Figure S5). The deviation is sensitive to the Far1 activation rate by Fus3, because its decrease disrupts the separation of timescales between the feedforward motif and the upstream MAPK. That is, if the upstream MAPK cascade were slow enough to be on the same timescale as the transcriptional timescale of the feedforward motif, the dynamics of Fus3 activity would have to be incorporated into an accurate mathematical analysis of the feedforward motif. The separation of timescales has been previously recognized as a means by which the dynamics of complicated biological networks can be simplified (Alon, 2007a; Atay and Skotheim, 2014). As for the other three

parameters, they directly affect the sharpness of the switch at the interface between the two pathways (Figure S5). Taken together, our computational model supports the hypothesis that the feedforward motif is effectively insulated from the cell cycle during pheromone arrest by a switch-like transition.

Bypassing Positive Feedback Switches Results in a Loss of Network Modularity

To experimentally test the predicted relationship between switches and modularity, we rewired the interface between the G1/S cell cycle and pheromone pathways to reduce how switch-like the transition is. To do this, we replaced endogenous FAR1 with an allele with the 92nd residue mutated from leucine to proline (FAR1-L92P) (Donic et al., 2015). This mutation generates an additional Cdk consensus phosphorylation site that likely increases the ability of cyclin-Cdk complexes to target Far1 for degradation. We predict that this will break modularity by making Far1 degradation responsive to even the low levels of cyclin-Cdk complexes present during arrest before the

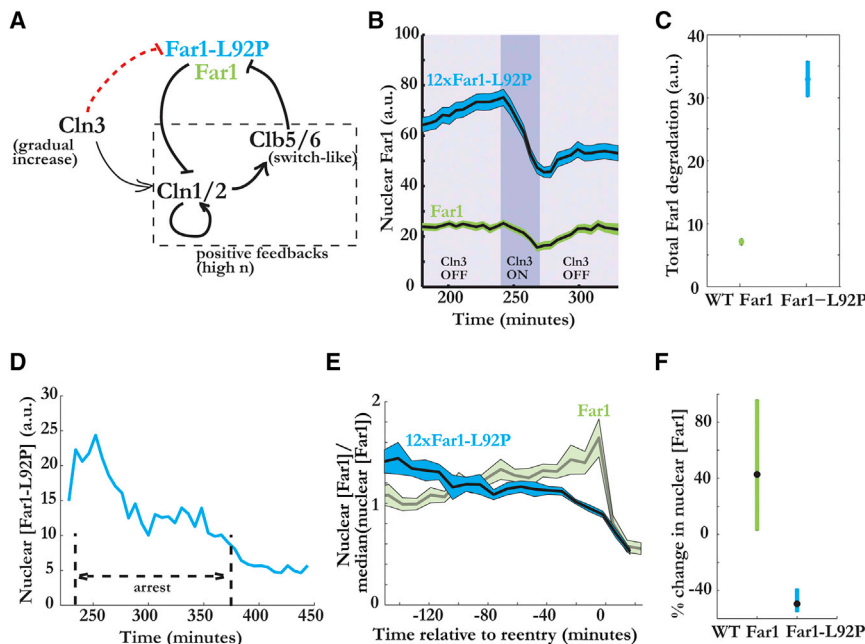


Figure 5. Mutation Sensitizing Far1 to Cyclin Expression Breaks Network Modularity

(A) Network schematic indicating likely effect of Far1-L92P mutation. The inhibition of Far1-L92P by Cln3 may be indirect.

(B) Nuclear Far1-GFP dynamics for *FAR1-GFP MET3pr-CLN3* and *12x*FAR1-L92P-GFP MET3pr-CLN3** cells that were arrested at 12 nM in the absence of Cln3 for 3 hr before being exposed to a 30 min pulse of Cln3. Importantly, this Cln3 pulse was not sufficient to drive cell-cycle reentry. Shaded region indicates the SEM.

(C) The mean nuclear Far1 degraded by the Cln3 pulse. Bars denote SEM for three biological replicates ($p < 0.001$).

(D and E) Example trace (D) and normalized means (E) of *12x*FAR1-L92P-GFP** cells exposed to a step increase from 0 to 3 nM pheromone. For comparison, we normalize and replot the data from Figure S1H for WT *FAR1-GFP* cells. Note that Cln3 in these cells is expressed from its endogenous locus. Traces are aligned at cell-cycle reentry and shaded region indicates the SE of the normalized means.

(F) Median percentage change in nuclear Far1 concentration during pheromone arrest for cells from (E) of the indicated genotype, calculated as

the difference between nuclear Far1 concentrations just before reentry and at the beginning of arrest. This difference is normalized by dividing with the nuclear Far1 concentration at the beginning of arrest. Bars denote the 90% confidence intervals computed using 10,000 bootstrap simulations ($p < 0.001$).

activation of the positive feedback loops (Figure 5A). Because the L92P mutation shortens half-life 2-fold to 3-fold during arrest and a single copy of *FAR1-L92P* does not arrest as readily as WT, we examined cells with ~ 12 copies, which arrest for similar durations as WT cells in response to pheromone (Doncic et al., 2015).

That the L92P mutation reduced Far1 half-life during arrest suggests that upstream cyclins can promote its degradation during arrest. To test this, we examined the response of *FAR1-GFP* and *12x*FAR1-L92P-GFP** cells expressing a pulse of Cln3. Importantly, this pulse of Cln3 was below the threshold required to trigger cell-cycle reentry. To do this, the endogenous *CLN3* promoter was replaced by the methionine-regulated *MET3pr* promoter (Charvin et al., 2008; Mao et al., 2002). Asynchronously dividing cells were exposed to 12 nM pheromone for 3 hr and then to 12 nM pheromone media lacking methionine to activate the expression of *MET3pr-CLN3* allele for 30 min. Then methionine was added back to the media to turn *MET3pr-CLN3* off. Throughout the experiment, we measured the dynamics of nuclear Far1-GFP expressed from either WT or L92P alleles. In WT cells, the decrease in Far1 was minimal (Figure 5B). Indeed, when Cln3 pulses were extended beyond 30 min, cells reentered the cell cycle and completely degraded their nuclear Far1 pool, suggesting that positive feedbacks that activate downstream cyclins Clb5/6 are triggered for longer Cln3 pulses. This is consistent with the feedforward motif being insulated from any changes in Cln3 expression until cell-cycle reentry in WT cells. In contrast, when this experiment was repeated using *12x*FAR1-L92P** cells, methionine-controlled Cln3 expression greatly reduced nuclear Far1 even when cells did not reenter the cell cycle (Figure 5B). In these experiments, more than four times as much Far1 was degraded in *12x*FAR1-L92P-GFP** cells compared with *FAR1-*

GFP cells (Figures 5C and S6). These experiments suggest that Far1-L92P dynamics are not insulated from changes in Cln3 expression in pheromone-arrested cells.

The sensitivity of Far1-L92P to sub-threshold levels of Cln3 suggests that modularity might be lost by the introduction of this mutation. To test this, we examined Far1 dynamics in *12x*FAR1-L92P** cells in which *CLN3* is now expressed from its native promoter. In these cells, Far1 levels gradually decreased during pheromone arrest until cell-cycle reentry (Figures 5D and 5E). This is consistent with non-modular motif analysis and our extended mathematical model with switch parameter $n = 1$ (compare Figures 5D and 5E with Figures S1E and 4D). Importantly, this contrasts with the observation of Far1 dynamics in WT cells and the prediction from the feedforward motif analysis, which both show that Far1 levels gradually increase until cell-cycle reentry (Figures 5F, S1B, and S1H). Taken together, these experiments demonstrate that the modularity of the feedforward motif is broken if upstream cyclin-Cdk complexes can target Far1 for degradation prior to cell-cycle reentry, that is, if the switch-like interface between the cell cycle and pheromone signaling is broken.

DISCUSSION

Although network motifs are commonly used to study signaling pathways, the validity of this approach and why it works as expected are unclear, because these motifs are always embedded in larger biological networks (Mellis and Raj, 2015). Here, we examine one specific case to find that motif-based analysis is valid only if the network is modular, that is, that the analyzed motif is insulated from other parts of the network. Motifs can be insulated from the effects of gradually changing inputs by

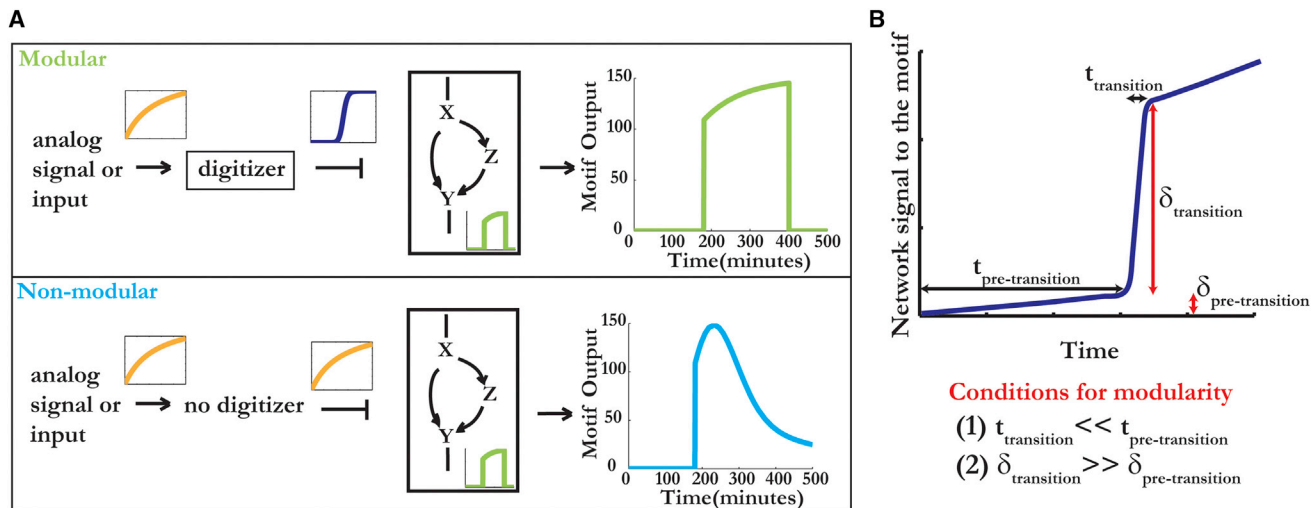


Figure 6. Summary Schematic

(A) Incorporation of switch-like elements that digitize signals enhances network modularity, which allows motif-based analysis. The expected motif dynamics (middle) match observed motif outputs (right) when a digitizer element insulates the motif from gradually changing analog inputs (modular case, top). In contrast, in the absence of such digitizer elements, analog signals can result in striking differences between expected and observed motif dynamics (non-modular case, bottom).

(B) For a transition to modularize a network, two conditions need to be met: (1) timescales of the transition must be much smaller than timescales of the period prior to the transition, and (2) the scale of the change through the transition must be larger than changes prior to the transition.

positive feedbacks, which can serve as digitizers that convert analog inputs into binary signals (Figure 6A). In the absence of such digitizers, motif dynamics deviate from the theoretical expectation because the activity of motif elements will be affected by changes elsewhere in the network.

Our analysis suggests that there are two requirements for a digitizer to modularize a network and insulate a motif from a changing input signal (Figure 6B). First, there needs to be a rapid transition. In the case of the feedforward motif, this means that the timescale of the reentry switch needs to be much faster than the timescale of arrest duration. Such a separation of timescales has been recognized as an important concept that allows the simplification of the mathematical analysis of complex biological phenomena (Alon, 2006, 2007a; Atay and Skotheim, 2014; Del Vecchio et al., 2008). Second, the change in output during the transition needs to be much larger than the change in output prior to the transition so that the output during arrest can be neglected. In the feedforward case we examined, this means that the change in the level of B-type cyclin activity during the cell-cycle switch must be significantly larger than its level during arrest.

Although the motif approach has limitations, the conditions under which it is valid may still be widespread in natural biological networks. This is because switch-like elements that modularize networks are likely widespread and not unique to the network comprising cell-cycle and pheromone pathways. Recent single-cell RNA sequencing studies of mammalian cells support this view (Jaatin et al., 2014; Treutlein et al., 2014). These studies show that the vast majority of cells exist in few well-defined transcriptional states. The absence of many cells in intermediate transcriptional states implies that transitions between these states are rapid and switch-like. In our case, network modularity can be thought to result from the existence of two

distinct cell states, the low-CDK activity state before the G1/S transition and the high-CDK activity state of being in the cell cycle. These two states are separated by a rapid positive feedback-driven transition so that from the point of view of the pheromone pathway, the cell-cycle state can be viewed as approximately binary (Skotheim et al., 2008). Because CDK in the low-activity state is largely unable to target Far1 for degradation, the feedforward motif is able to predict Far1 dynamics. This illustrates how, despite the apparent interconnectivity of many pathways, networks can be broken up into motifs insulated from the effects of changing inputs by the switches generating well-defined cellular states.

Consistent with this theme of insulation of different pathways, it was recently shown that although the yeast osmotic stress and pheromone-induced MAPK pathways share upstream components, these two signals are insulated from each other (Patterson et al., 2010). That is to say, activation of one pathway neither triggers nor interferes with signal propagation through the other pathway despite their shared components. This insulation is another facet of network modularity. However, although modularity is likely widespread, it is important to note that networks cannot be arbitrarily decomposed into motifs on the basis of network schematics. Still, our analysis suggests that positive feedback loops or any other known switch-like elements are good candidates for separating distinct modules.

Although it is generally difficult to say why biological networks should be modular, it is tempting to speculate in our specific case. Here, the insulation of Far1 from gradually increasing cell-cycle inputs ensures its stability on the timescale of cell growth. This, and the fact that the Far1 synthesis rate is determined by the current extracellular pheromone concentration, enables the current Far1 level to encode a memory of past pheromone exposure. A mutation (*FAR1-L92P*) that breaks modularity,

by allowing cell-cycle inputs to affect Far1 stability during arrest, also results in a loss of memory of past pheromone exposure (Doncic et al., 2015). Modularity may therefore have arisen because of selection for cellular memory. Although it was initially proposed that bistability was a property of the MAPK pathway per se, our work is consistent with later work concluding that MAPK activity responds in a graded fashion to extracellular pheromone (Takahashi and Pryciak, 2008; Yu et al., 2008). As shown here, bistability arises from the interaction of the MAPK and cell-cycle pathways. In our view, the graded MAPK response during pheromone arrest is important to allow the cell to measure duration and amplitude of pheromone exposure.

Here, we showed how network modularity isolates the feedforward motif, likely so that it can accurately process and remember dynamic pheromone signals. However, non-modular networks might also be able to perform this function. When networks were computationally evolved to perform a specific function, the resulting networks were often non-modular, and it was often not clear how a specific node might affect network function (Thompson, 1997). This work implies that additional selective pressures are likely required for the evolution of modular biological networks. One possibility is that modularity is a byproduct of selection for the switch-like transitions that allow cells to make rapid decisions and prevent mixed cellular states with severe fitness costs (Doncic et al., 2011; Strickfaden et al., 2007). A second possibility is that modularity itself may be selected for as a way to enhance network evolvability. Consistent with this notion, computational evolution studies have shown that alternating selection pressures result in modular networks (Kashtan and Alon, 2005). These selected networks tend to have distinct pathways to perform different functions that can be rapidly and independently tuned by mutation and selection. Interestingly, a recent computational study found that fluctuating selective pressures can result not only in increased evolvability, but also in increased nonlinearity and bistable dynamics (Kuwahara and Soyer, 2012). Thus, modularity, bistability, and evolvability may be deeply intertwined.

EXPERIMENTAL PROCEDURES

Strains and Media

All strains are derived from W303 and were constructed using standard methods (see Table S3). Strains were grown in yeast synthetic complete media lacking methionine with 2% glucose (SCD-methionine) unless otherwise indicated. All media were supplemented with 20 mg/ml casein to decrease α -factor surface adhesion to microfluidics plates.

Measurement of Fluorescent Proteins

Zeiss Observer Z1 microscope with a 63X/1.4NA oil immersion objective was used to take images every 6 min in all microscopy experiments. Media conditions were controlled using a CellASIC microfluidics device. Image segmentation, tracking and quantification was performed as described in Doncic et al. (2013). Autofluorescence in each imaging channel was determined and accounted for by imaging a control strain lacking the corresponding fluorescent fusion protein. Under the conditions used here, maturation kinetics and photobleaching were insignificant (Doncic et al., 2015; Schmoller et al., 2015) (see Supplemental Experimental Procedures for details).

Mathematical Modeling

Ordinary differential equation models were simulated in MATLAB using custom-written Runge-Kutta ODE solvers and with ode23t and ode23tb

ODE solvers for all mathematical modeling results. All mathematical models are described in detail in Supplemental Experimental Procedures.

SUPPLEMENTAL INFORMATION

Supplemental Information includes Supplemental Experimental Procedures, seven figures, and three tables and can be found with this article online at <http://dx.doi.org/10.1016/j.cels.2016.06.010>.

AUTHOR CONTRIBUTIONS

Conceptualization, O.A., A.D., and J.M.S.; Methodology, O.A., A.D., and J.M.S.; Investigation, O.A.; Formal Analysis, O.A.; Writing, O.A., A.D., and J.M.S.; Funding Acquisition, J.M.S.; Supervision, J.M.S.

ACKNOWLEDGMENTS

We thank Rainis Venta and Mart Loog for sharing the yeast strain RV200 and Daniel Fisher for his valuable input and critical reading of the manuscript. We also thank Ervin Valk and Mart Loog for sharing unpublished results describing the *FAR1-L92P* mutation. This work was supported by the Burroughs Wellcome Fund through a Career Award at the Scientific Interface (J.M.S.), the National Institutes of Health through grant R01 GM092925 (A.D. and J.M.S.), and a Stanford University Interdisciplinary Graduate Fellowship (O.A.).

Received: February 23, 2016

Revised: May 6, 2016

Accepted: June 20, 2016

Published: July 21, 2016

REFERENCES

- Alberghina, L., Rossi, R.L., Querin, L., Wanke, V., and Vanoni, M. (2004). A cell sizer network involving Cln3 and Far1 controls entrance into S phase in the mitotic cycle of budding yeast. *J. Cell Biol.* 167, 433–443.
- Alon, U. (2006). *An Introduction to Systems Biology: Design Principles of Biological Circuits* (Boca Raton: CRC Press).
- Alon, U. (2007a). Simplicity in biology. *Nature* 446, 497.
- Alon, U. (2007b). Network motifs: theory and experimental approaches. *Nat. Rev. Genet.* 8, 450–461.
- Atay, O., and Skotheim, J.M. (2014). Modularity and predictability in cell signaling and decision making. *Mol. Biol. Cell* 25, 3445–3450.
- Bardwell, L. (2004). A walk-through of the yeast mating pheromone response pathway. *Peptides* 25, 1465–1476.
- Basu, S., Mehreja, R., Thiberge, S., Chen, M.T., and Weiss, R. (2004). Spatiotemporal control of gene expression with pulse-generating networks. *Proc. Natl. Acad. Sci. U S A* 101, 6355–6360.
- Bhaduri, S., and Pryciak, P.M. (2011). Cyclin-specific docking motifs promote phosphorylation of yeast signaling proteins by G1/S Cdk complexes. *Curr. Biol.* 21, 1615–1623.
- Bhattacharyya, R.P., Reményi, A., Good, M.C., Bashor, C.J., Falick, A.M., and Lim, W.A. (2006). The Ste5 scaffold allosterically modulates signaling output of the yeast mating pathway. *Science* 311, 822–826.
- Boone, C., Bussey, H., and Andrews, B.J. (2007). Exploring genetic interactions and networks with yeast. *Nat. Rev. Genet.* 8, 437–449.
- Chang, F., and Herskowitz, I. (1990). Identification of a gene necessary for cell cycle arrest by a negative growth factor of yeast: FAR1 is an inhibitor of a G1 cyclin, CLN2. *Cell* 63, 999–1011.
- Charvin, G., Cross, F.R., and Siggia, E.D. (2008). A microfluidic device for temporally controlled gene expression and long-term fluorescent imaging in unperturbed dividing yeast cells. *PLoS ONE* 3, e1468.
- Chen, R.E., and Thorne, J. (2007). Function and regulation in MAPK signaling pathways: lessons learned from the yeast *Saccharomyces cerevisiae*. *Biochim. Biophys. Acta* 1773, 1311–1340.

- Costanzo, M., Nishikawa, J.L., Tang, X., Millman, J.S., Schub, O., Breitkreuz, K., Dewar, D., Rupes, I., Andrews, B., and Tyers, M. (2004). CDK activity antagonizes Whi5, an inhibitor of G1/S transcription in yeast. *Cell* 117, 899–913.
- de Bruin, R.A., McDonald, W.H., Kalashnikova, T.I., Yates, J., 3rd, and Wittenberg, C. (2004). Cln3 activates G1-specific transcription via phosphorylation of the SBF bound repressor Whi5. *Cell* 117, 887–898.
- Del Vecchio, D., Ninfa, A.J., and Sontag, E.D. (2008). Modular cell biology: retroactivity and insulation. *Mol. Syst. Biol.* 4, 161.
- Doncic, A., and Skotheim, J.M. (2013). Feedforward regulation ensures stability and rapid reversibility of a cellular state. *Mol. Cell* 50, 856–868.
- Doncic, A., Falleur-Fettig, M., and Skotheim, J.M. (2011). Distinct interactions select and maintain a specific cell fate. *Mol. Cell* 43, 528–539.
- Doncic, A., Eser, U., Atay, O., and Skotheim, J.M. (2013). An algorithm to automate yeast segmentation and tracking. *PLoS ONE* 8, e57970.
- Doncic, A., Atay, O., Valk, E., Grande, A., Bush, A., Vasen, G., Colman-Lerner, A., Loog, M., and Skotheim, J.M. (2015). Compartmentalization of a bistable switch enables memory to cross a feedback-driven transition. *Cell* 160, 1182–1195.
- Errede, B., and Ammerer, G. (1989). STE12, a protein involved in cell-type-specific transcription and signal transduction in yeast, is part of protein-DNA complexes. *Genes Dev.* 3, 1349–1361.
- Ferrell, J.E., Jr., and Xiong, W. (2001). Bistability in cell signaling: how to make continuous processes discontinuous, and reversible processes irreversible. *Chaos* 11, 227–236.
- Garrenton, L.S., Braunwarth, A., Imiger, S., Hurt, E., Künzler, M., and Thorner, J. (2009). Nucleus-specific and cell cycle-regulated degradation of mitogen-activated protein kinase scaffold protein Ste5 contributes to the control of signaling competence. *Mol. Cell. Biol.* 29, 582–601.
- Gartner, A., Jovanović, A., Jeoung, D.I., Bourlat, S., Cross, F.R., and Ammerer, G. (1998). Pheromone-dependent G1 cell cycle arrest requires Far1 phosphorylation, but may not involve inhibition of Cdc28-Cln2 kinase, in vivo. *Mol. Cell. Biol.* 18, 3681–3691.
- Gerhart, J. (1999). 1998 Warkany lecture: signaling pathways in development. *Teratology* 60, 226–239.
- Goranov, A.I., Cook, M., Ricicova, M., Ben-Ari, G., Gonzalez, C., Hansen, C., Tyers, M., and Amon, A. (2009). The rate of cell growth is governed by cell cycle stage. *Genes Dev.* 23, 1408–1422.
- Guet, C.C., Elowitz, M.B., Hsing, W., and Leibler, S. (2002). Combinatorial synthesis of genetic networks. *Science* 296, 1466–1470.
- Gyorgy, A., and Del Vecchio, D. (2014). Modular composition of gene transcription networks. *PLoS Comput. Biol.* 10, e1003486.
- Hartwell, L.H., Hopfield, J.J., Leibler, S., and Murray, A.W. (1999). From molecular to modular cell biology. *Nature* 402, C47–C52.
- Henchoz, S., Chi, Y., Catarin, B., Herskowitz, I., Deshaies, R.J., and Peter, M. (1997). Phosphorylation- and ubiquitin-dependent degradation of the cyclin-dependent kinase inhibitor Far1p in budding yeast. *Genes Dev.* 11, 3046–3060.
- Hussain, F., Gupta, C., Hirning, A.J., Ott, W., Matthews, K.S., Josic, K., and Bennett, M.R. (2014). Engineered temperature compensation in a synthetic genetic clock. *Proc. Natl. Acad. Sci. U S A* 111, 972–977.
- Jaitin, D.A., Kenigsberg, E., Keren-Shaul, H., Elefant, N., Paul, F., Zaretsky, I., Mildner, A., Cohen, N., Jung, S., Tanay, A., and Amit, I. (2014). Massively parallel single-cell RNA-seq for marker-free decomposition of tissues into cell types. *Science* 343, 776–779.
- Kashtan, N., and Alon, U. (2005). Spontaneous evolution of modularity and network motifs. *Proc. Natl. Acad. Sci. U S A* 102, 13773–13778.
- Köivomägi, M., Valk, E., Venta, R., Iofik, A., Lepiku, M., Balog, E.R.M., Rubin, S.M., Morgan, D.O., and Loog, M. (2011). Cascades of multisite phosphorylation control Sic1 destruction at the onset of S phase. *Nature* 480, 128–131.
- Kuwahara, H., and Soyer, O.S. (2012). Bistability in feedback circuits as a by-product of evolution of evolvability. *Mol. Syst. Biol.* 8, 564.
- Liu, X., Wang, X., Yang, X., Liu, S., Jiang, L., Qu, Y., Hu, L., Ouyang, Q., and Tang, C. (2015). Reliable cell cycle commitment in budding yeast is ensured by signal integration. *eLife* 4, e03977.
- Ma, W., Trusina, A., El-Samad, H., Lim, W.A., and Tang, C. (2009). Defining network topologies that can achieve biochemical adaptation. *Cell* 138, 760–773.
- MacArthur, B.D., Ma'ayan, A., and Lemischka, I.R. (2009). Systems biology of stem cell fate and cellular reprogramming. *Nat. Rev. Mol. Cell Biol.* 10, 672–681.
- Mangan, S., and Alon, U. (2003). Structure and function of the feed-forward loop network motif. *Proc. Natl. Acad. Sci. U S A* 100, 11980–11985.
- Mao, X., Hu, Y., Liang, C., and Lu, C. (2002). MET3 promoter: a tightly regulated promoter and its application in construction of conditional lethal strain. *Curr. Microbiol.* 45, 37–40.
- McKinney, J.D., and Cross, F.R. (1995). FAR1 and the G1 phase specificity of cell cycle arrest by mating factor in *Saccharomyces cerevisiae*. *Mol. Cell. Biol.* 15, 2509–2516.
- Mellis, I.A., and Raj, A. (2015). Half dozen of one, six billion of the other: What can small- and large-scale molecular systems biology learn from one another? *Genome Res.* 25, 1466–1472.
- Narula, J., Devi, S.N., Fujita, M., and Igoshin, O.A. (2012). Ultrasensitivity of the *Bacillus subtilis* sporulation decision. *Proc. Natl. Acad. Sci. U S A* 109, E3513–E3522.
- Norman, T.M., Lord, N.D., Paulsson, J., and Losick, R. (2013). Memory and modularity in cell-fate decision making. *Nature* 503, 481–486.
- Oehlen, L.J., McKinney, J.D., and Cross, F.R. (1996). Ste12 and Mcm1 regulate cell cycle-dependent transcription of FAR1. *Mol. Cell. Biol.* 16, 2830–2837.
- Patterson, J.C., Klimenko, E.S., and Thorner, J. (2010). Single-cell analysis reveals that insulation maintains signaling specificity between two yeast MAPK pathways with common components. *Sci. Signal.* 3, ra75.
- Perrimon, N., Pitsouli, C., and Shilo, B.Z. (2012). Signaling mechanisms controlling cell fate and embryonic patterning. *Cold Spring Harb. Perspect. Biol.* 4, a005975.
- Pope, P.A., Bhaduri, S., and Pryciak, P.M. (2014). Regulation of cyclin-substrate docking by a G1 arrest signaling pathway and the Cdk inhibitor Far1. *Curr. Biol.* 24, 1390–1396.
- Regot, S., Macia, J., Conde, N., Furukawa, K., Kjellén, J., Peeters, T., Hohmann, S., de Nadal, E., Posas, F., and Solé, R. (2011). Distributed biological computation with multicellular engineered networks. *Nature* 469, 207–211.
- Schmoller, K.M., Turner, J.J., Köivomägi, M., and Skotheim, J.M. (2015). Dilution of the cell cycle inhibitor Whi5 controls budding-yeast cell size. *Nature* 526, 268–272.
- Schwob, E., and Nasmyth, K. (1993). CLB5 and CLB6, a new pair of B cyclins involved in DNA replication in *Saccharomyces cerevisiae*. *Genes Dev.* 7 (7A), 1160–1175.
- Schwob, E., Böhm, T., Mendenhall, M.D., and Nasmyth, K. (1994). The B-type cyclin kinase inhibitor p40SIC1 controls the G1 to S transition in *S. cerevisiae*. *Cell* 79, 233–244.
- Skotheim, J.M., Di Talia, S., Siggia, E.D., and Cross, F.R. (2008). Positive feedback of G1 cyclins ensures coherent cell cycle entry. *Nature* 454, 291–296.
- Strickfaden, S.C., Winters, M.J., Ben-Ari, G., Lamson, R.E., Tyers, M., and Pryciak, P.M. (2007). A mechanism for cell-cycle regulation of MAP kinase signaling in a yeast differentiation pathway. *Cell* 128, 519–531.
- Takahashi, S., and Pryciak, P.M. (2008). Membrane localization of scaffold proteins promotes graded signaling in the yeast MAP kinase cascade. *Curr. Biol.* 18, 1184–1191.
- Thompson, A. (1997). An evolved circuit, intrinsic in silicon, entwined with physics. In *Evolvable Systems: From Biology to Hardware* (New York: Springer), pp. 390–405.
- Treutlein, B., Brownfield, D.G., Wu, A.R., Neff, N.F., Mantalas, G.L., Espinoza, F.H., Desai, T.J., Krasnow, M.A., and Quake, S.R. (2014). Reconstructing lineage hierarchies of the distal lung epithelium using single-cell RNA-seq. *Nature* 509, 371–375.

- Tsang, J., Zhu, J., and van Oudenaarden, A. (2007). MicroRNA-mediated feed-back and feedforward loops are recurrent network motifs in mammals. *Mol. Cell* 26, 753–767.
- Tsutsui, H., Karasawa, S., Okamura, Y., and Miyawaki, A. (2008). Improving membrane voltage measurements using FRET with new fluorescent proteins. *Nat. Methods* 5, 683–685.
- Tyers, M., Tokiwa, G., Nash, R., and Fletcher, B. (1992). The Cln3-Cdc28 kinase complex of *S. cerevisiae* is regulated by proteolysis and phosphorylation. *EMBO J.* 11, 1773–1784.
- Yang, X., Lau, K.Y., Sevim, V., and Tang, C. (2013). Design principles of the yeast G1/S switch. *PLoS Biol.* 11, e1001673.
- Yosef, N., and Regev, A. (2011). Impulse control: temporal dynamics in gene transcription. *Cell* 144, 886–896.
- Yu, R.C., Pesce, C.G., Colman-Lerner, A., Lok, L., Pincus, D., Serra, E., Holl, M., Benjamin, K., Gordon, A., and Brent, R. (2008). Negative feedback that improves information transmission in yeast signalling. *Nature* 456, 755–761.

Cell Systems, Volume 3

Supplemental Information

**Switch-like Transitions Insulate Network Motifs
to Modularize Biological Networks**

Oguzhan Atay, Andreas Doncic, and Jan M. Skotheim

Supplementary Material

Supplemental Experimental Procedures, related to Materials and Methods

Wide-Field Time Lapse Microscopy

Zeiss Observer Z1 microscope with a 63X/1.4NA oil immersion objective was used to take images every 6 minutes in all microscopy experiments. Multiple positions were imaged using an automated stage and Axiovision software, and Definite Focus hardware was used for automated focal plane alignment during time-lapse experiments. Media conditions and changes were controlled using a Cellasic microfluidics device with Y04C plates. Prior to loading, cells were grown overnight at 30°C to $OD_{600} < 0.1$ and then sonicated for ~5-10 s at 3 W intensity. In order to avoid cell-density effects, all strains examined lack the Bar1 protease that cleaves extracellular mating pheromone (Ballensiefen and Schmitt, 1997). GFP, mCitrine, mKok, and mCherry expressing strains were exposed for 150 ms, 400 ms, 750 ms, and 750 ms using Colibri 470, 505, 550, or 540-80 LED modules respectively. All Colibri modules were used at 25% power except for mCherry, which was used at 50% power. Image segmentation, tracking and quantification was conducted as described in Doncic et al, 2013. There is no significant photobleaching under these exposure conditions and the fusion of *FAR1*, *WHI5*, *CLN3*, and *SIC1* to these fluorescent proteins has previously been shown not to affect their activities (Doncic et al., 2015; Schmoller et al., 2015; Yang et al., 2013).

Measurement of fluorescent proteins

To measure nuclear Far1-GFP and Far1-L92P-GFP concentrations, we first fit a Gaussian to the Whi5-mKok signal to find the nucleus. Since commitment to cell cycle is molecularly defined as the point at which ~50% of Whi5 is exported from the nucleus, Whi5 is nuclear during pheromone arrest and serves as a marker for both arrest and nuclear location (Doncic et al., 2011). Using Whi5 as a marker for nuclear location, we measured the average GFP signal intensity in the nucleus. While this GFP signal is a proxy for Far1 levels, it needs to be corrected for cell growth to accurately reflect relative nuclear Far1 concentrations over longer time scales. Since cells grow during arrest, their z-dimension increases, which results in an increase in autofluorescence as well as a slight increase in the z-dimension of the nucleus. To find the size-dependent autofluorescence, we arrested a control strain not expressing GFP in pheromone and measured the autofluorescence signal in the GFP channel as cells grew. Then, we fit a linear regression to find the relationship between cell thickness, given by volume/area, and autofluorescence in the GFP channel. We then subtracted the size-dependent autofluorescence signal from the GFP signal intensity. We note that we also subtracted the non-cell background signal, which can vary slightly from one microfluidics plate to another. We then divided this background subtracted intensity signal by the cell thickness to find the nuclear Far1 concentration signal.

For the other fluorescent proteins, mCitrine-Cln3-11A, Whi5-mKok, GFP driven by the *CLB5* promoter, and Sic1-GFP, we similarly found and subtracted the size-dependent autofluorescence in their respective channels by arresting each background strain in pheromone using the same exposure

conditions as tagged strains and finding the relation between cell size and autofluorescence at different cell sizes for each channel. Note that because different fluorescent channels display relatively different dependencies of autofluorescence on size, different linear equations were fit for each channel. We also note that since active and inactive fractions of Far1 cannot be distinguished *in vivo*, ‘nuclear [Far1]’ refers to the concentration of total nuclear Far1 in all experiments while it refers to the active fraction in the panels that refer to the model, unless otherwise indicated.

Time scales were calculated as the time required to reach half-maximum or half-minimum of any observable changes that would drive cell cycle reentry. This corresponds to the time required to reach half-maximum volume from the start of the arrest, time required to reach half-maximum level for Cln3 from the start of an arrest, the time required to reach half-maximum levels for GFP expressed from the *CLB5* promoter after promoter firing, and the time required to degrade half of the existing pools of Sic1 and nuclear Far1. For average traces, single cell traces were first aligned at the point that this change starts for each marker, *i.e.*, at the beginning of the arrest for volume and Cln3, at the time of promoter firing near cell cycle reentry for the *CLB5* promoter, and at the time of cell cycle reentry for Sic1 and Far1 proteins. Then, fluorescent values were binned based on time, and mean and standard error of the mean for fluorescent concentrations were calculated within each bin. We note that maturation kinetics of fluorophores does not significantly impact our calculation of time scales. This is because maturation primarily results in a delay, which does not change the time to reach half-maximum for a transition. While the standard deviation of the distribution of maturation times may be expected to slightly smoothen a transition and result in the observed kinetics to be slower than actual kinetics, simulations with first-order kinetics suggest that this would minimally affect time to half-maximum that we calculated (<3 min for even lowly expressed proteins (~500 molecules at the end of the transition) tagged with slow maturing fluorophores (~30 min).

We note that for the pulse experiment shown in Figure 2, 60-minute 3 nM gaps were chosen because longer gaps or lower pheromone concentrations typically result in most cells reentering the cell cycle in the first gap. This is because the fraction of total Far1 that is phosphorylated and active is significantly lower at lower pheromone concentrations.

For all experiments, only daughter cells that are born during pheromone arrest and reenter the cell cycle during the experiment are chosen for analysis. The number of daughter cells selected for each experiment varies between 15 and 120. While all our conclusions also hold for mother cells, they are omitted from these analyses because their arrest durations are significantly shorter due to cell type-specific factors (Caudron and Barral, 2013; Di Talia et al., 2009).

Derivation of analytical form of nuclear Far1 in modular and non-modular networks

In this section, we solve for Far1 in the feedforward motif model to show how Far1 dynamics would differ if the feedforward motif is insulated (modular network) or not (non-modular network). To derive the analytical form for Far1_{nuc} levels for a modular network (Figure S1A), we follow Donicic and Skotheim (2013) with minor modifications to account for reentry to cell cycle and enrichment of nuclear Far1 as discussed in Donicic et al (2015). If the cell is arrested, Far1 is

synthesized by active Ste12 at a rate k_s , and Far1 has a constant half-life determined by k_{dg} . Thus, the total Far1 concentration, including phosphorylated and nonphosphorylated fractions, is given by:

$$\frac{d[Far1_{tot}]}{dt} = k_s [Ste12] - k_{dg} [Far1_{tot}]. \quad \text{Eq. 1}$$

Since phosphorylation and dephosphorylation kinetics are fast, active Ste12 is determined by instantaneous Fus3 kinase activity. Since Fus3 activity is in turn determined by phosphorylation events upstream in the MAPK pathway, we take Fus3 activity and thereby Ste12 activity to be a function of instantaneous extracellular pheromone concentration, $p(t)$. Therefore,

$[Ste12] = g(Fus3(p(t))) = F(p(t))$. So that:

$$\frac{d[Far1_{tot}]}{dt} = k_s F(p(t)) - k_{dg} [Far1_{tot}], \quad \text{Eq. 2}$$

which can be integrated to yield:

$$[Far1_{tot}] = [Far1_0]e^{-k_{dg}t} + \int_0^t k_s F(p(t'))e^{-k_{dg}(t-t')} dt', \quad \text{Eq. 3}$$

where $[Far1_0]$ represents the initial pool of Far1 at $t = 0$, which is when the cell is born and arrest begins. We note that $[Far1_0]$ is sufficiently high so that when it is phosphorylated and activated, it is able to arrest cells. At any time, only a fraction of the total $Far1_{tot}$ is activated by phosphorylation. At a much faster time-scale than synthesis and cell growth, the non-phosphorylated form of Far1 is phosphorylated by Fus3 at a rate k_p while phosphorylated Far1 is dephosphorylated at a rate k_{dp} , so that the phosphorylated form of Far1 is given by:

$$\frac{d[Far1_p]}{dt} = k_p ([Far1_{tot}] - [Far1_p])[Fus3] - k_{dp} [Far1_p]. \quad \text{Eq. 4}$$

We note that Fus3 is abundant and therefore unlikely to be saturated (Thomson et al., 2011). Since the phosphorylation kinetics of Eq. 4 are faster than the synthesis kinetics of Eq. 3, $Far1_p$ is at steady state on the slower synthesis time scale. At steady state, Eq. 4 yields:

$$[Far1_p] = \frac{[Fus3]}{\frac{k_{dp}}{k_p} + [Fus3]} [Far1_{tot}]. \quad \text{Eq. 5}$$

Moreover, Far1 is transported to the nucleus at the start of the arrest and is enriched in nucleus, compared to the cytoplasm during arrest. We assume that Far1 nuclear transport is faster than synthesis so that we can represent the spatial organization of phosphorylated Far1 using a nuclear-to-cytoplasmic ratio k_n : $[Far1_{nuc}] = k_n [Far1_p]$. If a cell reenters the cell cycle (Whi5 cytoplasmic), the motif no longer is functional and nuclear Far1 is completely degraded so that $Far1_{nuc} = 0$. Incorporating this into Eqn. 3 and 5, we find:

$$Far1_{nuc} = \begin{cases} \frac{k_n [Fus3(p(t))]}{\frac{k_{dp}}{k_p} + [Fus3(p(t))]} ([Far1_0]e^{-k_{dg}t} + \int_0^t k_s F(p(t'))e^{-k_{dg}(t-t')} dt'), & \text{if Whi5 nuclear} \\ 0, & \text{if Whi5 cytoplasmic} \end{cases} \quad \text{Eq. 6}$$

Note that for the result shown in Figure S1B, Equation 1 is numerically solved, instead of explicitly integrated. Active [Fus3(p(t))] is estimated as:

$$[Fus3(t)] = \frac{[Fus3_{max}]}{K_f + \exp(-\log_{10}(p(t)/nM))}, \quad \text{Eq. 7}$$

where $K_f = 1$ so that pheromone concentration for half-maximum Fus3 concentration is 1 nM, consistent with published measurements (Figure S7A) (Yu et al., 2008). We take $[Fus3_{max}] = 200$ nM, which corresponds to ~ 5000 molecules per cell and is consistent with previous estimates (Maeder et al., 2007; Slaughter et al., 2007; Thomson et al., 2011). Then, the synthesis rate of Far1 as a function of pheromone is estimated as:

$$k_s \cdot Ste12(t) = k_s \cdot F(p(t)) = k_s (A + B (1 - \exp(-\frac{p(t)}{10 \text{ nM}}))), \quad \text{Eq. 8}$$

so that Far1 synthesis is significantly increased only at high α -factor concentrations, consistent with previous measurements ($A = 70$ nM; $B = 130$ nM) (Figure S7B) (Doncic and Skotheim, 2013).

To complete the model, additional parameters were chosen as follows: $[Far1_0] = 60$ nM; $\frac{k_{dp}}{k_p} = 10$ nM; $k_n = 2$; $k_s = 0.01 \text{ min}^{-1}$; $k_{dg} = 0.01 \text{ min}^{-1}$.

For a modular network, Far1 is not targeted for degradation by cyclins prior to cell cycle reentry, and the Far1 degradation rate, k_{dg} , is a constant low value, which is a result of the combined effect of dilution due to growth and the effect of constitutive (non-specific) degradation (Figure S1C).

In a non-modular network, Far1 would be inhibited by increasing cell cycle signal (Figure S1D). To incorporate increasing degradation of Far1 by cell cycle inputs, k_{dg} was modified to be a linearly increasing function of time instead of being set to a constant value ($k_{dg} = c t$, where $c = 0.0002 \text{ min}^{-2}$ for the simulation shown in Figure S1D,E). For both non-modular and modular analyses of the feedforward motif, the Far1 half-life is $\ln(2)/k_{dg}$ (Figure S1C,F). Note that for the modular network, because $[Far1_{nuc}]$ drops to zero following cell cycle reentry, $k_{dg} \rightarrow \infty$, so that $Far1_{1/2} \rightarrow 0$.

Intuitive explanation of Far1 feedforward motif model

If the feedforward motif is a module, then its dynamics can be studied in isolation from other interactions in the network. Thus, we first look at what the feedforward motif model predicts in absence of any interacting components. In our model here, we also focus on the active nuclear pool of Far1 because it determines cell cycle arrest (Doncic et al., 2015). The initial jump in nuclear Far1 when cells arrest is due to rapid nuclear import of cytoplasmic Far1, which is more stable throughout the cell cycle and can accumulate in S/G2/M phases despite high Cdk activity (Figure S1B) (Doncic et al., 2015). This initial pool of Far1 is also rapidly activated by phosphorylation, allowing cells not yet committed to division to quickly respond to pheromone and arrest. Nuclear Far1 is a relatively constant fraction of total Far1 (Doncic et al., 2015), and, as with total Far1, Fus3 activity determines the active fraction of nuclear Far1. We consequently take the concentration of

the active nuclear pool to be a constant multiple of phosphorylated and activated total Far1 in this model.

Phosphorylation and dephosphorylation are both rapid processes so that Fus3 and Ste12 are taken to be a function of the extracellular pheromone concentration, $p(t)$, as measured in (Yu et al., 2008). Then, the amount of phosphorylated Far1 is determined by the total Far1, $Far1_{tot}$, active Fus3, and Far1 phosphorylation and dephosphorylation rates, k_p and k_{dp} , respectively, so that: $[Far1_p] = \frac{[Far1_{tot}][Fus3]}{[Fus3] + k_{dp}/k_p}$. At intermediate pheromone concentrations, total Far1 slowly increases from its relatively high initial value to reach a constant steady state value, $[Far1_{tot}^*]$, that balances production by Ste12 with Far1 degradation: $[Far1_{tot}^*] = k_s [Ste12]/k_{dg}$, where k_s is the Far1 synthesis rate and k_{dg} is the Far1 degradation rate. Importantly, because this model does not account for any inhibitory cell cycle signal, Far1 activity does not gradually decrease prior to cell cycle reentry. Instead, cell cycle reentry is modeled as the point at which the motif no longer functions. Thus, in the modular analysis, Far1 half-life is constant until cell cycle reentry (Figure S1C).

In contrast, if the feedforward motif is not a module, the cell cycle signal would influence Far1 stability and concentration (Figure S1D). As the cells get larger during pheromone arrest, the cell cycle signal is expected to gradually increase, leading to increasing Far1 degradation. When this degradation is incorporated into the above model, Far1 follows a dramatically different trajectory where it gradually decreases during arrest (Figure S1E,F). Thus, if the cell cycle signal is not insulated from the pheromone pathway, Far1 dynamics will be very different from the modular feedforward motif prediction.

Analysis of the effect of switch-like transitions on the modularity of the network comprising the G1/S cell cycle and pheromone pathways

While the simplified model described above and in Figure S1 provides an intuition for how network modularity can impact feedforward motif dynamics, it does not explicitly model the pheromone pathway cell cycle interface. We therefore constructed a slightly more complex model that allows us to analyze how parameters affecting the interface between dynamic cell cycle inputs and the feedforward motif determine network modularity. We emphasize that the purpose of this model is not to recapitulate the accurate dynamics for G1/S network or pheromone pathway but rather to investigate the conditions for network modularity. That is why many cell cycle components are omitted in this model, and many complexities such as the compartmentalization of Far1 into cytoplasmic and nuclear pools and the separate behavior of these pools due to nuclear localization of cyclins are greatly simplified. For more molecularly complete models we refer the interested reader to studies focusing on either the complete cell cycle or pheromone pathways (Kofahl and Klipp, 2004; Kraikivski et al., 2015; Tyson and Novák, 2015; Wang et al., 2006; Yao et al., 2008).

The ODE model adds a simplified cell cycle pathway model to the feedforward motif (see Results and Figure 4 for an intuitive explanation of the model). Volume is taken to be increasing slowly and linearly, as measured in Figure 3A,B:

$$\frac{d(volume)}{dt} = k_1 \quad \text{Eq. 9}$$

This linear increase in size is transmitted to Cln3, and Cln3 also gradually increases, but with a saturation kinetics that is similar to that measured in Figure 3C,D.

$$\frac{d[Cln3]}{dt} = \frac{k_2 \text{ volume}}{K_v + \text{volume}} - d_1 [Cln3], \quad \text{Eq. 10}$$

where k_2 is a scaling constant for maximum Cln3 synthesis rate, K_v is the volume required to reach half-maximum Cln3 synthesis rate, and d_1 is the degradation rate of Cln3. Here and also for other cyclins, cyclin-Cdk complex formations are not explicitly modeled since these interactions are rapid and that Cdk1, the only Cdk in yeast, is in excess (Cross et al., 2002). While Cln3 drives cell-cycle reentry primarily by inhibiting Whi5 (Costanzo et al., 2004; de Bruin et al., 2004), the model does not explicitly consider this interaction since Whi5 is relatively constant in pheromone-arrested cells at intermediate pheromone concentrations (Figure 3E,F). Furthermore, Whi5 inactivation results in Cln1 and Cln2 activation, which is also not explicitly modeled here because Cln1 and Cln2 were shown to have little effect on the kinetics of cell cycle reentry from pheromone arrest (Doncic and Skotheim, 2013). On the other hand, B-type cyclins affect reentry kinetics and Clb5 has been shown to target Far1 for degradation, indicating that it is the activation of B-type cyclins that drive the dismantling of the feedforward motif (Doncic et al., 2015). We therefore construct a simplified model in which Cln3 activates B-type cyclin expression with Michaelis-Menten-type kinetics, and B-type cyclins can also activate their own expression, either gradually or sharply. Clb5/6 denotes the cyclin-Cdk complexes that are not bound to the inhibitor proteins Sic1 and Far1. Cyclin-Cdk complexes bound to inhibitors are denoted by FC. Assuming that the rate at which cyclins bind Cdk is fast, the amount of active cyclin-Cdk complexes is given by:

$$\begin{aligned} \frac{d[Clb5/6]}{dt} = & \frac{k_3 [Cln3]}{K_G + [Cln3]} + \frac{k_4 [Clb5/6]^n}{K_B^n + [Clb5/6]^n} - k_5 [Far1_p][Clb5/6] \\ & + k_6 [FC] + k_7 [FC] - k_{dg} [Clb5/6], \end{aligned} \quad \text{Eq. 11}$$

where k_3 and k_4 are the scaling constants for the maximum activation rate of B-type cyclins by Cln3 and by themselves, respectively, K_B is the B-type cyclin concentration required to reach half-maximum self-activation rate, K_G is the Cln3 concentration required to reach half-maximum B-type cyclin activation rate due to Cln3, and k_{dg} represents the constitutive degradation rate of Clb5/6 (inverse half-life). Here, it must be noted that the switch-like nature of Clb5/6 auto-activation embodies all the positive feedbacks between Cln3 and Clb5/6, including that potentially arising from Cln1 and Cln2 and B-type cyclin activity promoting the degradation of the B-type cyclin inhibitor Sic1 (Köivomägi et al., 2011; Skotheim et al., 2008). Also, since these differential equations describe the time-derivatives of a protein concentration, the second term in Eqn. 11 does not technically correspond to the input-output relation that a Hill equation is often used to describe. However, the resulting behavior is the same. For increasing n , Clb5/6 is increasingly switch-like. We assume that Far1 and Clb5/6 interact with mass action kinetics. They form an inactive complex, FC, at a rate $k_5[Far1_p][Clb5/6]$. In turn, FC can separate into Far1_p and Clb5/6 at a relatively small rate k_6 , or FC

can separate into active Clb5/6 with Far1 being degraded at a rate of k_7 , or FC can separate into Far1_p with Clb5/6 being degraded at a rate of k_8 . Thus, the rate of change of the inactive complex FC is given by:

$$\frac{d[FC]}{dt} = k_5 \text{Far1}_p \text{Clb5/6} - k_6 FC - k_7 FC - k_8 FC - k_{dg} FC \quad \text{Eq. 12}$$

Since phosphorylation and dephosphorylation kinetics are taken to be much faster than the dynamics simulated in this ODE model, Fus3 and Ste12 activity is taken to be at steady state so that their levels are functions of only extracellular pheromone concentration and given by Eqns. 6 and 7, respectively as in the motif analysis above. Since phosphorylated Far1 is a fraction of total Far1 and is determined by current Fus3 concentration, we also assume that only phosphorylated Far1 can interact with Clb5/6 and use Eqn. 1, as in the motif analysis, to determine changes in total Far1 concentration. Then, phosphorylated and nuclear Far1 is the same as for the motif analysis (see Eq. 3) except for the Far1-Clb5/6 interaction terms. Thus:

$$\begin{aligned} \frac{d[\text{Far1}_p]}{dt} = & k_p([\text{Far1}_{tot}] - [\text{Far1}_p])[\text{Fus3}] - k_{dp}[\text{Far1}_p] \\ & - k_5[\text{Far1}_p][\text{Clb5/6}] + (k_6 + k_8)[FC] - k_{dg}\text{Far1}_p \end{aligned} \quad \text{Eq. 13}$$

$$\text{Far1}_{nuc} = k_n \text{Far1}_p. \quad \text{Eq. 14}$$

Here, we note that we did not include the effect of inhibition of MAPK scaffold protein Ste5 by Cdk activity because the dissociation of Ste5 from the plasma membrane occurs after nuclear Far1 is degraded (Doncic et al., 2011; Garrenton et al., 2009; Strickfaden et al., 2007). We also note that we have previously measured the median half-life of Far1 in pheromone-arrested cells and found it to be 100 minutes (Doncic and Skotheim, 2013), on the same time scale as dilution due to cell growth when cells are initially arrested. Thus, when cells are first arrested, both dilution and degradation contribute to decreasing the concentration of Far1. However, as cells increase in size during arrest, the amount of time to double cell mass increases in proportion to the current size because of the linear growth. Thus, after ~100 minutes of arrest, when cells have doubled in size, the effect of dilution will be reduced by a factor of two and the effect of degradation will increasingly dominate. To simplify the model, we use a single exponential term for degradation to reflect loss of Far1 in Eqs. 1, 2, 6 and 13. Other variables in the model are treated similarly.

As discussed in the main text, instead of trying to fit parameters and initial conditions to limited data, we choose parameters expected to be the correct order-of-magnitude based on our knowledge of cellular reaction rates. This allows us to gain a qualitative understanding of how different reactions underlie network modularity. All initial conditions and parameter values are listed in Supplementary Table S1 and S2.

Sensitivity analysis

To determine whether the deviation of Far1 dynamics from the idealized motif dynamics is sensitive to parameter values, we modified each parameter separately by randomly drawing 100 samples from

a Gaussian distribution with mean equal to the initial parameter value, and standard deviation equal to 1/3 of the initial parameter value. We found that only 4 parameters significantly affected the model deviation from the result predicted by an isolated feedforward motif model. These parameters were the switch parameter n , the B-type cyclin required to reach half-maximum self-activation rate K_B , Far1 degradation rate from the inactive complex k_7 , and Far1 phosphorylation rate k_p (Figure S5).

Note of the relationship between growth rate and modularity

Modularity is most likely unaffected by cell growth in yeast because most proteins are produced in proportion to total protein synthesis so that their concentrations are the same in big and small cells (Newman et al., 2006). For example, we previously found that the Far1 synthesis rate was relatively constant over a 2-3 hour cell cycle arrest in constant pheromone concentration (Doncic and Skotheim, 2013). This is consistent with the notion that the regulators of Far1 synthesis, Ste12, Dig1, and Dig2, remain at constant concentration as cells grow so that all their activities can be subsumed into a single parameter characterizing pheromone-dependent Ste12 activity. In addition, the relative amount of expression from most yeast promoters was shown to be independent of cell growth rate in a variety of conditions (Keren et al., 2013). This results in most proteins remaining at constant concentration in a variety of conditions without feedback control, which is rare in budding yeast (Springer et al., 2010; Tang and Amon, 2013). Thus, in a wide variety of conditions, in large and small cells, most signaling protein concentrations are expected to remain nearly constant so that most signaling modules will respond similarly.

Supplementary Tables

Table S1: Initial conditions for simulations shown in Figure 4, S3-S5. p is the extracellular pheromone concentration, which is constant in these simulations, unless otherwise indicated.

Variable	Description	Initial Condition	Units
Fus3	Active protein	$200/(1 + \exp(-\log_{10}(p)))$	nM
Ste12	Active protein	$70 + 130 (1 - \exp(-p/10))$	nM
Far1 _{tot}	Total protein	60	nM
Far1 _p	Phosphorylated protein	0	nM
Volume	Cell volume	40	fl
Cln3	Active protein	1	nM
Clb5/6	Active protein	0	nM
FC	Inactive Far1-Clb5/6 complex	0	nM

Table S2: Parameters for simulations shown in Figure 4, S3-S5

Rate	Description	Value	Units
k_s	Far1 Ste12-dependent synthesis rate	0.01	min ⁻¹
k_{dg}	Far1 constitutive degradation rate	0.01	min ⁻¹
k_p	Far1 phosphorylation rate by Fus3	0.005	nM ⁻¹ min ⁻¹
k_{dp}	Far1 constitutive dephosphorylation rate	0.05	min ⁻¹
k_n	Far1 nuclear-to-cytoplasmic ratio	2	
k_1	Volume increase rate	0.5	fl min ⁻¹
k_2	Scaling constant for maximum Cln3 synthesis rate	1.0	nM ⁻¹ min ⁻¹
K_v	Volume to reach half-maximum Cln3 synthesis rate	100	fl
d_1	Cln3 degradation rate	0.1	min ⁻¹
k_3	Scaling constant for maximum activation rate of B-type cyclin synthesis by Cln3	2	nM ⁻¹ min ⁻¹
k_4	Scaling constant for maximum activation rate of B-type cyclins by B-type cyclins (positive feedback)	25	nM ⁻¹ min ⁻¹
K_G	Cln3 concentration required to reach half-maximum B-type cyclin activation rate due to Cln3	10	nM
K_B	Clb5/6 concentration required to reach half-maximum self-activation rate	5	nM
n	Switch-parameter	1-8	
k_5	Rate of inactive [FC] formation	0.02	nM ⁻¹ min ⁻¹
k_6	Rate of [FC] break-up into [Far1 _p] and [Clb5/6]	0.01	min ⁻¹
k_7	Far1 degradation rate from [FC]	0.05	min ⁻¹
k_8	Clb5/6 degradation rate from [FC]	0.005	min ⁻¹

Table S3: Strain list, related to Materials and Methods

All strains are derived from W303 using standard methods.

Name	Genotype	Source
OA040	<i>MATa bar1::URA3 WHI5-mKok-TRP1 far1::kanMX-FAR1pr-FAR1-GFP-LEU2 ADE2</i>	(Doncic et al., 2015)
OA042	<i>MATa bar1::URA3 WHI5-mKok-TRP1 far1::kanMX-12x-FAR1pr-FAR1(L92P)-GFP-LEU2 ADE2</i>	(Doncic et al., 2015)
OA043	<i>MATa bar1::URA3 WHI5-mKok-TRP1 far1::kanMX-FAR1pr-FAR1-GFP-LEU2 MET3pr-CLN3-HIS ADE2</i>	This study
OA044	<i>MATa bar1::URA3 WHI5-mKok-TRP1 far1::kanMX-12x-FAR1pr-FAR1(L92P)-GFP-LEU2 MET3pr-CLN3-HIS ADE2</i>	This study
OA064	<i>MATa bar1::URA3 cln3::mCitrine-CLN3-11A-natMX6 ADE2</i>	This study
AD30-17c	<i>MATa bar1::natMX6 MET3pr-CLN2-TRP CLB5pr-GFP-URA WHI5-GFP-kanMX6</i>	This study
RV200	<i>MATa bar1::HISG sic1::SIC1-GFP-kanMX6 WHI5-mCherry-SpHIS5</i>	Rainis Venta

References

- Ballensiefen, W., and Schmitt, H.D. (1997). Periplasmic Barl Protease of *Saccharomyces Cerevisiae* is Active Before Reaching its Extracellular Destination. *European Journal of Biochemistry* *247*, 142-147.
- Caudron, F., and Barral, Y. (2013). A super-assembly of Whi3 encodes memory of deceptive encounters by single cells during yeast courtship. *Cell* *155*, 1244-1257.
- Costanzo, M., Nishikawa, J.L., Tang, X., Millman, J.S., Schub, O., Breitkreuz, K., Dewar, D., Rupes, I., Andrews, B., and Tyers, M. (2004). CDK activity antagonizes Whi5, an inhibitor of G1/S transcription in yeast. *Cell* *117*, 899-913.
- Cross, F.R., Archambault, V., Miller, M., and Klovstad, M. (2002). Testing a mathematical model of the yeast cell cycle. *Mol. Biol. Cell* *13*, 52-70.
- de Bruin, R.A., McDonald, W.H., Kalashnikova, T.I., Yates, J., and Wittenberg, C. (2004). Cln3 activates G1-specific transcription via phosphorylation of the SBF bound repressor Whi5. *Cell* *117*, 887-898.
- Di Talia, S., Wang, H., Skotheim, J.M., Rosebrock, A.P., Fitcher, B., and Cross, F.R. (2009). Daughter-specific transcription factors regulate cell size control in budding yeast. *PLoS Biology* *7*, 2375.
- Doncic, A., Atay, O., Valk, E., Grande, A., Bush, A., Vasen, G., Colman-Lerner, A., Loog, M., and Skotheim, J.M. (2015). Compartmentalization of a Bistable Switch Enables Memory to Cross a Feedback-Driven Transition. *Cell* *160*, 1182-1195.
- Doncic, A., Eser, U., Atay, O., and Skotheim, J.M. (2013). An algorithm to automate yeast segmentation and tracking. *PLoS One* *8*, e57970.
- Doncic, A., Falleur-Fettig, M., and Skotheim, J. (2011). Distinct Interactions Select and Maintain a Specific Cell Fate. *Mol. Cell* *43*, 528-539.
- Doncic, A., and Skotheim, J.M. (2013). Feedforward Regulation Ensures Stability and Rapid Reversibility of a Cellular State. *Mol. Cell* *50*, 856-868.
- Garrenton, L.S., Braunwarth, A., Irniger, S., Hurt, E., Kunzler, M., and Thorner, J. (2009). Nucleus-specific and cell cycle-regulated degradation of mitogen-activated protein kinase scaffold protein Ste5 contributes to the control of signaling competence. *Mol. Cell. Biol.* *29*, 582-601.
- Keren, L., Zackay, O., Lotan-Pompan, M., Barenholz, U., Dekel, E., Sasson, V., Aidelberg, G., Bren, A., Zeevi, D., Weinberger, A., *et al.* (2013). Promoters maintain their relative activity levels under different growth conditions. *Mol. Syst. Biol.* *9*, 701.
- Kofahl, B., and Klipp, E. (2004). Modelling the dynamics of the yeast pheromone pathway. *Yeast* *21*, 831-850.
- Kõivomägi, M., Valk, E., Venta, R., Iofik, A., Lepiku, M., Balog, E.R.M., Rubin, S.M., Morgan, D.O., and Loog, M. (2011). Cascades of multisite phosphorylation control Sic1 destruction at the onset of S phase. *Nature* *480*, 128-131.
- Kraikivski, P., Chen, K.C., Laomettachit, T., Murali, T., and Tyson, J.J. (2015). From START to FINISH: computational analysis of cell cycle control in budding yeast. *Npj Systems Biology and Applications* *1*, 15016.
- Maeder, C.I., Hink, M.A., Kinkhabwala, A., Mayr, R., Bastiaens, P.I., and Knop, M. (2007). Spatial regulation of Fus3 MAP kinase activity through a reaction-diffusion mechanism in yeast pheromone signalling. *Nat. Cell Biol.* *9*, 1319-1326.

- Newman, J.R.S., Ghaemmaghami, S., Ihmels, J., Breslow, D.K., Noble, M., DeRisi, J.L., and Weissman, J.S. (2006). Single-cell proteomic analysis of *S. cerevisiae* reveals the architecture of biological noise. *Nature* *441*, 840-846.
- Schmoller, K.M., Turner, J., Kõivomägi, M., and Skotheim, J.M. (2015). Dilution of the cell cycle inhibitor Whi5 controls budding-yeast cell size. *Nature* *526*, 268-272.
- Skotheim, J.M., Di Talia, S., Siggia, E.D., and Cross, F.R. (2008). Positive feedback of G1 cyclins ensures coherent cell cycle entry. *Nature* *454*, 291-296.
- Slaughter, B.D., Schwartz, J.W., and Li, R. (2007). Mapping dynamic protein interactions in MAP kinase signaling using live-cell fluorescence fluctuation spectroscopy and imaging. *Proc. Natl. Acad. Sci. U. S. A.* *104*, 20320-20325.
- Springer, M., Weissman, J.S., and Kirschner, M.W. (2010). A general lack of compensation for gene dosage in yeast. *Mol. Syst. Biol.* *6*, 368.
- Strickfaden, S.C., Winters, M.J., Ben-Ari, G., Lamson, R.E., Tyers, M., and Pryciak, P.M. (2007). A mechanism for cell-cycle regulation of MAP kinase signaling in a yeast differentiation pathway. *Cell* *128*, 519-531.
- Tang, Y., and Amon, A. (2013). Gene copy-number alterations: a cost-benefit analysis. *Cell* *152*, 394-405.
- Thomson, T.M., Benjamin, K.R., Bush, A., Love, T., Pincus, D., Resnekov, O., Yu, R.C., Gordon, A., Colman-Lerner, A., Endy, D., and Brent, R. (2011). Scaffold number in yeast signaling system sets tradeoff between system output and dynamic range. *Proc. Natl. Acad. Sci. U. S. A.* *108*, 20265-20270.
- Tyson, J.J., and Novák, B. (2015). Models in biology: lessons from modeling regulation of the eukaryotic cell cycle. *BMC Biology* *13*, 46.
- Wang, X., Hao, N., Dohlman, H.G., and Elston, T.C. (2006). Bistability, stochasticity, and oscillations in the mitogen-activated protein kinase cascade. *Biophys. J.* *90*, 1961-1978.
- Yang, X., Lau, K., Sevim, V., and Tang, C. (2013). Design principles of the yeast G1/S switch. *PLoS Biol* *11*, e1001673.
- Yao, G., Lee, T.J., Mori, S., Nevins, J.R., and You, L. (2008). A bistable Rb-E2F switch underlies the restriction point. *Nat. Cell Biol.* *10*, 476-482.
- Yu, R.C., Pesce, C.G., Colman-Lerner, A., Lok, L., Pincus, D., Serra, E., Holl, M., Benjamin, K., Gordon, A., and Brent, R. (2008). Negative feedback that improves information transmission in yeast signalling. *Nature* *456*, 755-761.

Supplementary Figures

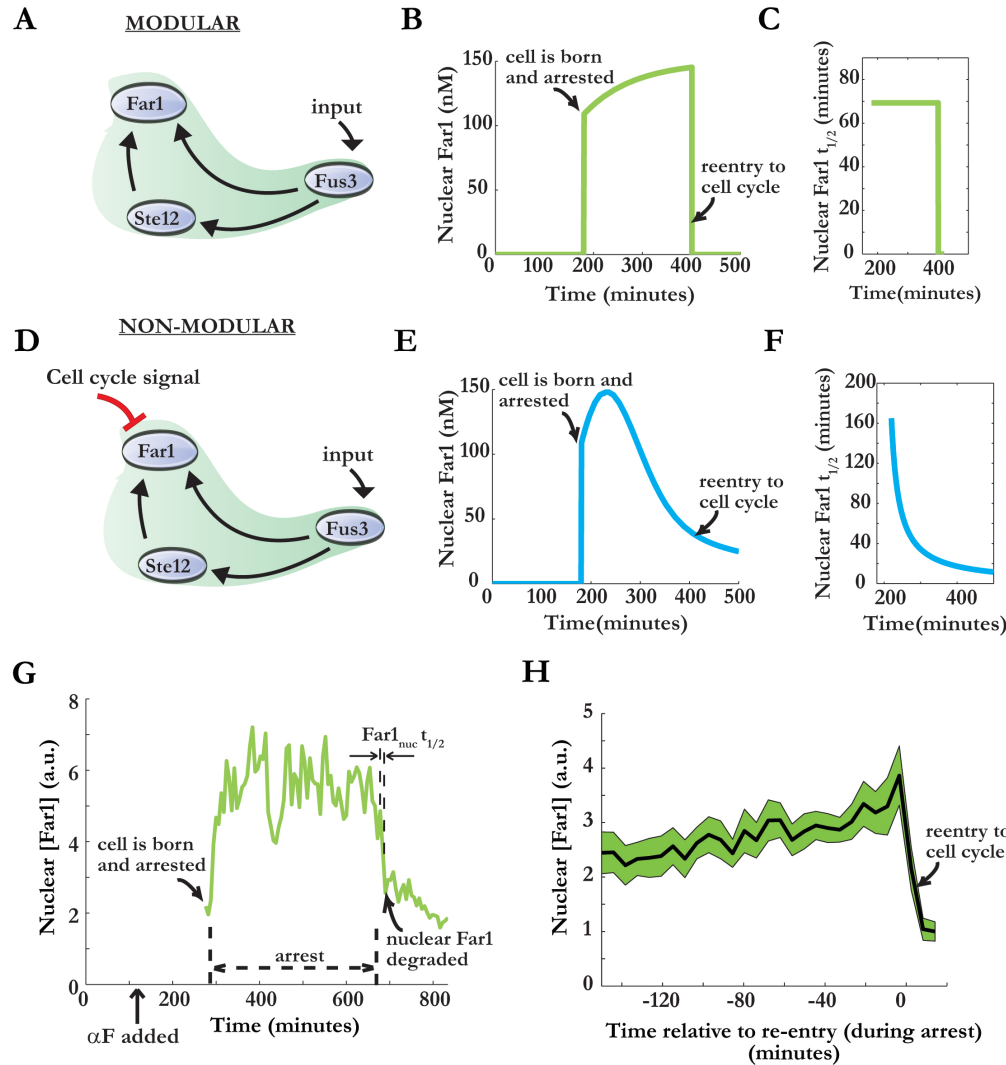


Figure S1: Far1 dynamics suggests that the network comprising the G1/S cell cycle and pheromone pathways is modular, related to Figure 2

(A-C) Nuclear Far1 dynamics predicted by an isolated analysis of the feedforward motif. In the absence of any cell cycle signals, Far1 level would be determined solely by the feedforward motif. Because inhibition of Far1 by gradually increasing cell cycle inputs is ignored until cell cycle reentry, Far1 half-life is constant until cell cycle reentry (C), at which point it is instantly degraded.

(D-F) Nuclear Far1 dynamics predicted by a non-modular model in which the gradually increasing cell cycle inputs lead to a gradual decrease in Far1 half-life. In this simulation, nuclear Far1 half-life is a monotonically decreasing function of time (F).

(G-H) Nuclear Far1 concentrations were measured in single *FAR1-GFP* cells exposed to a step-increase pheromone from 0 to 3 nM. (G) Nuclear Far1 concentration trace for an example cell, and (H) mean nuclear Far1 after all traces were aligned at cell cycle reentry and cell-specific Far1 background was subtracted. While the non-modular model predicted a gradual decrease of Far1 during arrest, the nuclear Far1 concentration slightly increased during arrest before its rapid degradation upon cell cycle reentry. Shaded intervals indicate standard error of the mean.

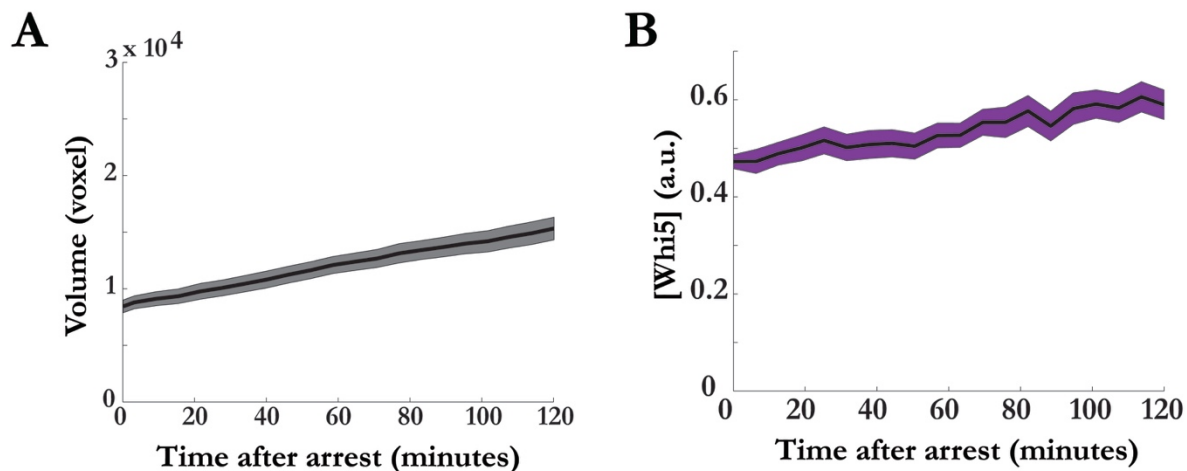


Figure S2: Whi5 concentration can increase at saturating pheromone concentrations, related to Figure 3.

(A) Mean volume and associated standard error for single cells aligned at the start of a 12nM pheromone arrest. Volume increase is slower at higher pheromone concentrations; compare with the first 2 hours of arrest in Figure 3B.

(B) Mean concentration and associated standard error for the cell cycle inhibitor Whi5-mKok for cells arrested in 12nM pheromone. Whi5 concentration increased in cells exposed to 12 nM pheromone; compare with the first 2 hours of arrest in Figure 3F.

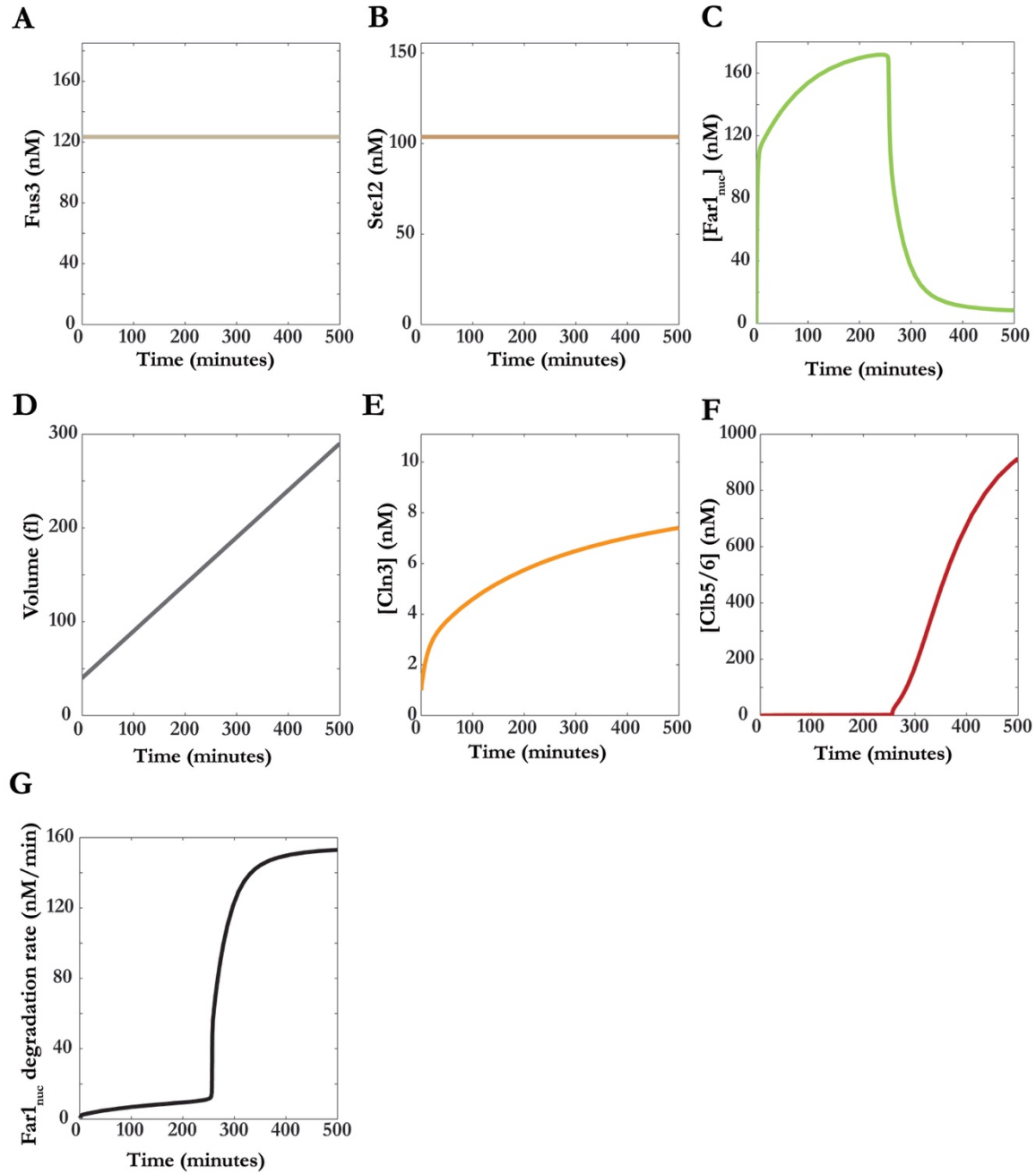


Figure S3: The kinetics of different proteins in the model presented in Figure 4.

(A-F) Simulation results for switch parameter $n=6$, pheromone $p=3$ nM. Initial conditions and parameters are as shown in Table S1 and Table S2 respectively.

(G) Nuclear Far1 degradation rate during the simulation. The sharp increase is due to Clb5/6 activity.

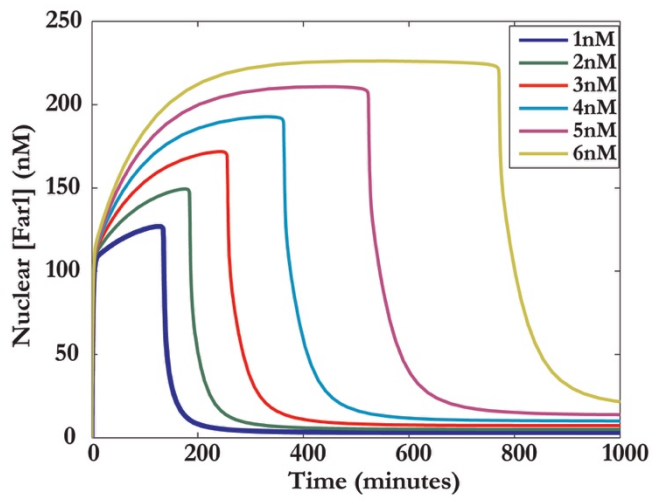


Figure S4: The effect of pheromone concentration on reentry timing, related to Figure 4. Switch parameter $n = 6$. Initial conditions and parameters are as shown in Table S1 and Table S2 respectively. Pheromone concentration was constant during the simulation.

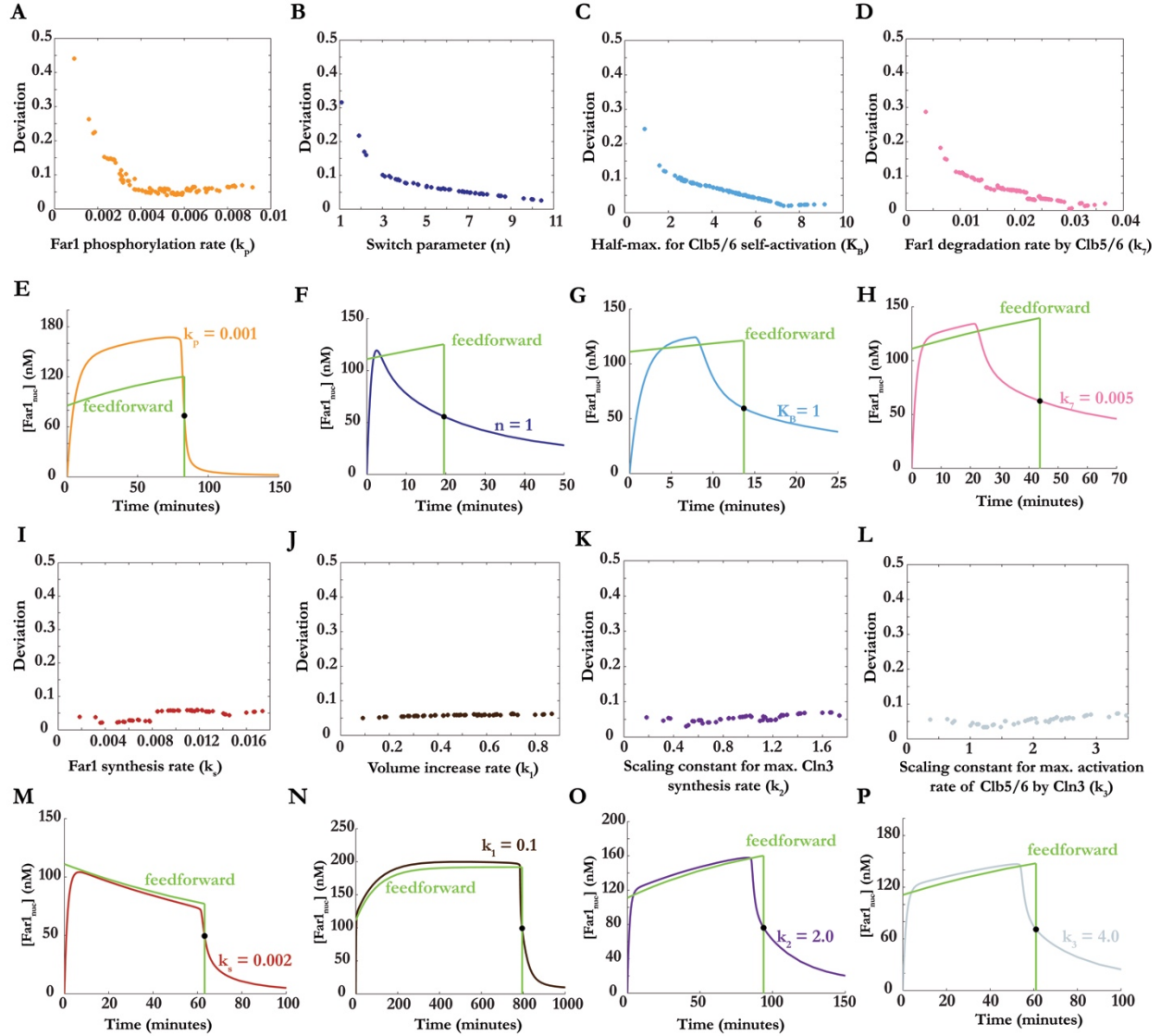


Figure S5: Parameter sensitivity analysis, related to Figure 4. Simulations were performed as in Figure 4, but with varying parameters. For all simulations except those shown in (B) and (F), the switch parameter $n = 6$ and initial conditions are given in Table S1. With the exception of the indicated varied parameter, the parameters are as shown in Table S2 respectively. A set of values for each parameter was selected by randomly drawing 100 samples from a Gaussian distribution with mean equal to the initial parameter value, and standard deviation equal to $1/3$ of the initial parameter value. Then, for each value in the set, a simulation was performed and the deviation from the isolated feedforward model calculated.

(A-D) Deviation from the isolated feedforward model as a function of the 4 sensitive parameters.

(E-H) Example traces indicating how model results deviate from the isolated feedforward model for the indicated sensitive parameters.

(I-P) Comparable sensitivity analysis as in (A-H) for 4 parameters that do not significantly impact the deviation from the isolated feedforward model. When a parameter that affected the isolated feedforward model was varied, the feedforward model was also simulated using the varied parameter. Similar results were obtained for the remaining 8 parameters that are not shown here.

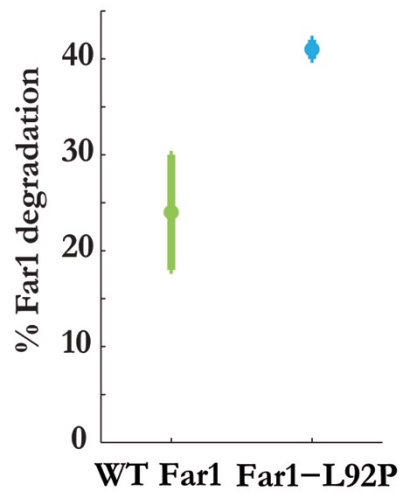


Figure S6: Percentage of Far1 degraded by a Cln3 pulse, related to Figure 5. For the experiment shown in Figure 5B, but instead of mean Far1 degradation as in Figure 5C, percentage of Far1 degraded by the Cln3 pulse is calculated. The error bars denote the standard error of the mean for three biological replicate experiments ($p < 0.05$).

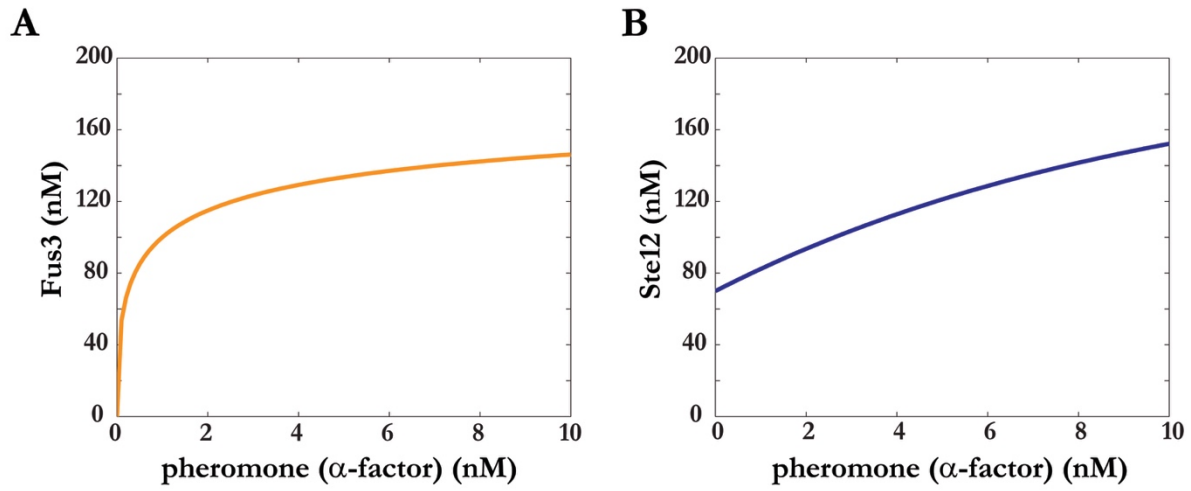


Figure S7: Functions showing how Fus3 and Ste12 activity depends on pheromone concentration, related to Supplementary Material and Figure 4. Plots of equations 7 and 8 for Fus3 (A) and Ste12 (B) respectively.